ISSN 2543-9901

JOURNAL OF CASTING & MATERIALS ENGINEERING

QUARTERLY
Vol. 6 No. 2/2022

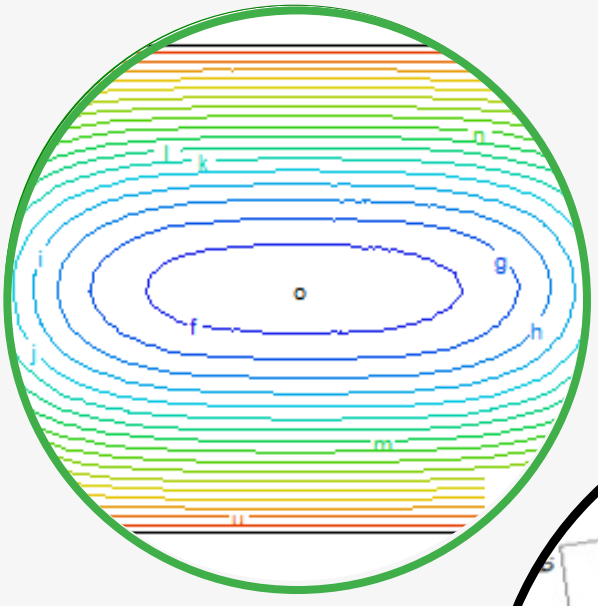

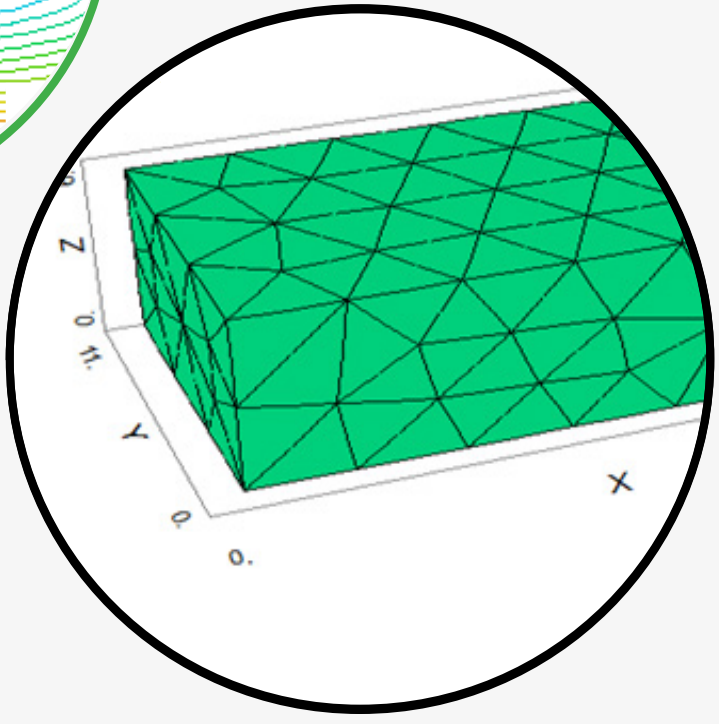

JCME

AGH UNIVERSITY PRESS
KRAKOW 2022

AGH UNIVERSITY OF SCIENCE AND TECHNOLOGY
FACULTY OF FOUNDRY ENGINEERING

The articles published in the Journal of Casting & Materials Engineering have been given a favorable opinion by the rewievers designated by the Editorial Board.

www:
https://journals.agh.edu.pl/jcme/

AGH UNIVERSITY PRESS KRAKOW 2022

Wydawnictwa AGH (AGH University Press)
al. A. Mickiewicza 30, 30-059 Kraków
tel. 12 617 32 28, 12 638 40 38
e-mail: redakcja@wydawnictwoagh.pl
http://www.wydawnictwa.agh.edu.pl

Contents

Journal of Casting & Materials Engineering Vol. 6 No. 2 (2022) 33–38
https://doi.org/10.7494/jcme.2022.6.2.33

A Novel Approach to Quantifying the Effect of the Density of Sand Cores on Their Gas Permeability

Dinesh Sundaram*, József Tamás Svidró, Judit Svidró, Attila Diószegi

Jönköping University School of Engineering, Department of Materials and Manufacturing, Gjuterigatan 5, Box 1026, SE-55111 Jönköping, Sweden
**email: dinesh.sundaram@ju.se*

Received: 29 October 2021/Accepted: 22 February 2022/ Published online: 30 March 2022.
This article is published with open access at AGH University of Science and Technology Press.

Abstract

The density of moulding mixtures used in the foundry industry plays a significant role since it influences the strength, porosity, and permeability of moulds and cores. The latter is routinely tested in foundries using different solutions to control the properties of the moulding materials that are used to make moulds and cores. In this paper, the gas permeability of sand samples was measured using a custom-made setup to obtain the gas permeability in standard units instead of the usual permeability numbers (PN) with calibrated units. The aim of the work was to explore the effect of density variations in moulding materials on their gas permeabilities. Permeability in this work is quantified in SI units, square metres [m^2]. The setup works based on Darcy's law and the numbers obtained from the measurements can be used to deduce the gas permeability, *k*, of a sample. Two furan resin bonded mixtures with the same grain size distribution were hand-rammed with varying compaction forces to obtain a variation in density. Cylindrical samples (50 × 50 mm) were prepared using a silica sand aggregate sourced from a Swedish lake. The results of the measurement provided the difference in gas permeability between the samples that have varying densities. The results of permeability were then extrapolated by modifying the viscosity value of the air passed through the sample. In order to find the effect of apparent density variation on the pore characteristics of the samples, mercury intrusion porosimetry (MIP) was also performed. The results were in line with the gas permeability measurements.

Keywords:

compaction, density, furan sand, gas permeability, porous media

1. INTRODUCTION

Sand casting, one of the oldest and most versatile manufacturing processes, involves pouring molten metal into a mould cavity that is designed and shaped according to the structure and dimensions of the finished form of the component [1]. Casting methods using aggregates can be divided into two main types: non-permanent molds made by permanent patterns or non-permanent patterns. Of these two, high volume production is achieved using non-permanent/expendable moulds with permanent patterns [1]. Cores are parts of these moulds that serve the purpose of creating hollow cavities or shapes inside the cavity where patterns cannot be used [2]. Cores are prepared by binding aggregate material either using organic or inorganic binder. They are usually accompanied by the addition of a catalyst material depending on the type of the resin and process. Since they involve multiple components, they are termed binder systems [3].

Hand-ramming is an important process in the foundry industry for small volume production and prototyping. It involves the manual compaction of sand grains already mixed with the binding agents. The role of compaction or ramming is significant for several reasons. Among other things, compaction determines the density, and permeability of the moulding material. Smaller cores are compacted by compressed air and, for larger moulds and cores, pneumatic rammers are commonly used. On the industrial scale, machine compaction methods such as compression, injection and core shooting are used. Moulds are commonly manufactured using methods like bench moulding (for low production rates), machine moulding (high volume production), pit moulding (large castings) and floor moulding (medium sized castings) [4]. During the casting process, the moulds and cores must withstand heat shock and pressure in the system. If the gases formed during the thermal decomposition find a way to the liquid metal, gas related defects such as blow holes will appear in the casting. Hence gas-permeability of cores and moulds affects the casting quality and is a critical parameter [5]. In this work, the density of furan no-bake sand cores was varied by altering the compaction force during hand ramming. Gas permeability was measured using a custom-made measurement setup that provides numbers in standard units of square metres [m^2].

2. BACKGROUND

The density of sand used for foundry purposes are measured in different forms. Loose, dry and free flowing sand bulk density is measured using a 100 ml graduated cylinder and the procedure for testing this parameter is provided by the AFS Mold and Core Test Handbook [6]. On the other hand, the apparent density of solid moulds is measured using the direct relationship between the mass and the volume of the moulds and cores. Gas permeability of moulds are dependent on several factors. On a micro-scale, properties of the sand grains like the grain size and shape influence the permeability. On a macroscopic level, properties of the mould/core such as the apparent density and the resulting porosity of the sample influence the permeability. In this study, the compaction force was varied while preparing samples to achieve a difference in the apparent density, and the resulting differences in gas permeability this variation caused was quantified.

Gas permeability has not been modelled extensively for foundry cores and moulds. Several researchers from other fields have worked on predicting the gas permeability of sandstones, soil and other rocks using parameters such as grain size distribution, porosity etc. [7, 8]. Permeability prediction from porosimetry data has also been widely carried out in other fields, such as earth sciences and geothermal engineering. Ettemeyer et al. [7] measured the gas permeability of foundry cores that are 3D-printed. In their work, the measured gas permeability data were used to predict the behaviour of the sand cores, when high temperature gases passed through them.

Dańko et al. [9] studied the core properties prepared from core shooters using a custom method. Of the properties that were studied, the effect of shooting pressure, rate of filling, and the apparent density were the primary focus for different sand grain types. In another related work, Dańko worked on establishing the effect of grain size distribution on the bending strength and apparent density of commercially shot foundry samples [10]. It is also known from research in the field of petrochemical and geothermal sciences that permeability is more dependent on the pore characteristics than the porosity itself. In consolidated media there could be instances where samples that may be more porous but could have lesser interconnected pores and therefore having lower gas permeability [11]. The authors of the current work performed mercury intrusion porosimetry (MIP) measurements to reveal the pore characteristics of furan no-bake cores in an earlier study. In that work the authors quantified the effect of grain size distribution on the gas permeability of foundry cores and identified a certain threshold limit for the permeability after which the reduction in permeability were not significant [12]. The authors also identified the importance of pore characteristics of furan no-bake cores and its effect on the gas permeability. In the current work presented, the effect of apparent density on the gas permeability were studied. It is important to quantify the pore characteristics of a porous material, because they play a significant role on the gas transport properties of the sample and hence it is analysed using MIP in this study.

3. MATERIALS AND METHODS

For this study, foundry grade silica sand sourced from a Swedish lake was used as the aggregate material. The sand is widely used by the foundry industry in Sweden. The grain size distribution is shown in Figure 1. The grain size distribution and the average grain size were determined according to Swedish standards.

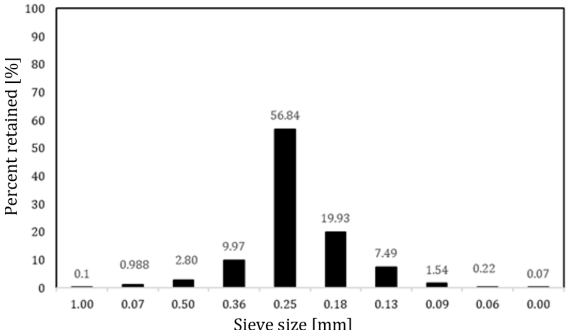

Fig. 1. Grain size distribution of the silica sand used

2% (of the mass of sand) of furan resin was added to the sand along with 40% (of the mass of the resin) sulphonic acid-based catalyst and mixed. The mixture was then hand-rammed with a custom-made rammer and tube setup. A known mass of sand was inputted into the tubes and the compaction force was varied such that the density of the samples also varied. The compaction force was not measured. The samples prepared were of the standard cylindrical geometry (50 × 50 mm) that is used widely for foundry sand testing. The curing time was 24 hours for both samples. The properties of the samples are shown in Table 1.

Table 1
Properties of the samples prepared and measured for permeability

Sample	Mass [g]	Volume [cm^3]	Density [g/cm^3]	Average grain size [mm]
A	135.12	99.73	1.39	0.31
B	149.62	99.83	1.51	

The samples were evaluated in three steps. First, gas permeability measurements were conducted using a custom-made setup that utilizes Darcy's law. The cylindrical core is enclosed in an air-tight setup that allows air (at room temperature) to flow through the specimen from one end to the other end. The pressure difference building up was measured using a differential pressure sensor. The velocity of the air was also measured on the outlet side using a mass flow sensor. The working principle and more detailed governing calculations can be found in a previous work published [13].

In the second step, the obtained gas permeability numbers were used to reveal the hypothetic effect of temperature on the gas permeability of the samples. This provides information about how the sand mixture might behave when the

temperature of the passing gas is higher (which is close to the reality when it comes to casting processes). However, the calculation assumes that the decomposition of the furan resin does not have an effect on the pore characteristics, since the resin and catalyst content is low both in mass and volume fraction when compared to the sand grains. This assumption has been previously made by researchers while measuring gas permeability [14, 15].

In the third step, the samples were then analysed using mercury intrusion MIP, using a Micro metrics Autopore III 9410.

This method provided data on the porosity, pore size distribution, pore area and other important pore characteristics. The 50 × 50 mm, cylindrical samples were cut, and three specimens from the central area of each cylinder were then machined out, according to Figure 2.

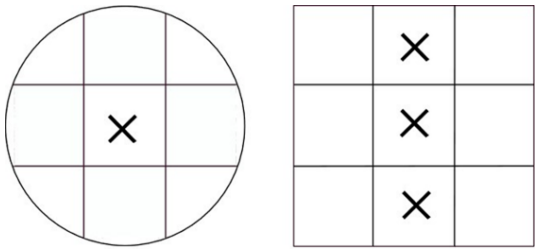

Fig. 2. Cylindrical samples were cut and the pieces for the MIP marked with a cross mark

4. RESULTS AND DISCUSSION

4.1. Permeability results

The ratio of volumetric flow rate of the air, Q in cubic metres on seconds that is measured at the outlet to the cross-sectional area, A in in squar metres of the sample is plotted (x-axis) as a function of the ratio of the differential pressure, dP in Pascals to the length of the sample, L in meters in the y-axis. Q/A plotted against dP/L for the two samples are superimposed and shown in Figure 3. From the slope of these plots, gas permeability is calculated with the help of the dynamic viscosity of air. The dynamic viscosity of the air that is passed through the sample is 1.85E-5 kg/ms [16]. A total of four measurements were performed for each sample studied and the mean with the standard deviation was calculated. The standard deviation numbers for these measurements could be found in Table 2.

The slope of the sample A is visibly steeper and has a higher gas permeability. This is expected as Sample A has a density of 1.39 g/cm^3 and it is the lower of the two samples studied. The slope of sample B is smaller than the slope of A. Sample B had a density of 1.51 g/cm^3. The air flow rate per unit area is lesser for sample B and shows that the sample is less permeable. The gas permeability values of the measured samples are presented in Figure 4. The mean gas permeability and the standard deviation results are presented in Table 2.

It can be seen that the standard deviation for sample B was much higher than Sample A. The results show that the gas permeability for Sample A was higher with $5.26 \cdot 10^{-12}$ m^2 as the mean value of four measurements. Gas-permeability of Sample B which had a higher density, eventuated in lower gas-permeability of $1.43 \cdot 10^{-12}$ m^2. The background of these findings were evaluated further by means of MIP tests.

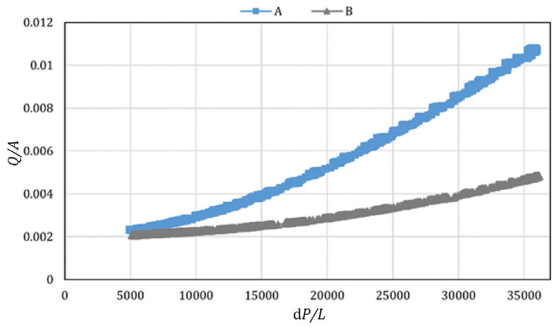

Fig. 3. Volumetric flow rate divided by the area of cross-section of the sample(y-axis)plotted against the differential pressure divided by the length of the sample

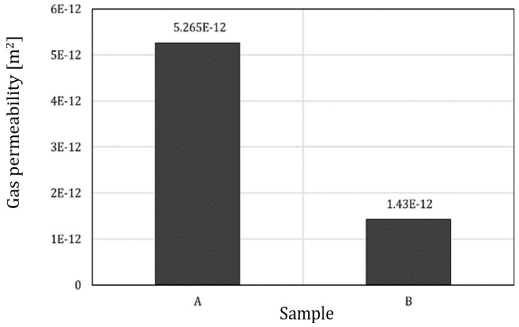

Fig. 4. Gas permeability of the measured samples A and B

Table 2
The mean gas permeability and the standard deviation results

Parameter	Sample A	Sample B
Apparent density [g/cm^3]	1.39	1.51
Gas permeability [m^2]	5.265E-12 ±0.09	1.43E-12 ±0.18
Measurement 1	5.14E-12	1.61992E-12
Measurement 2	5.24E-12	1.19667E-12
Measurement 3	5.29E-12	1.61045E-12
Measurement 4	5.39092E-12	1.34216E-12

4.2. Permeability calculated for higher temperatures based on Darcy's law

Darcy's law provides a proportionality between the volumetric flow rate of a porous material and the pressure gradient of the material when a fluid passes through [17]. The law also includes the dimensions of the sample measured such as

the area of the sample and length. Since fluid viscosity plays a significant role in the flow characteristics, the law also includes dynamic viscosity. Darcy's law can be written as in following equation, where k/μ can be obtained from the plots presented in Figure 3.

$$\frac{Q}{A} = \frac{k}{\mu} \cdot \frac{dP}{L}$$

where:

Q – volumetric flow rate of air;
A – cross-sectional area of the sample;
k – permeability;
μ – dynamic viscosity;
dP – differential pressure across the sample;
L – length of the sample.

The dynamic viscosity μ at room temperature [16] was used to determine the gas permeability of the material. To study the effect of fluid temperature on the gas permeability, the dynamic viscosity for higher temperatures [16] was considered and are incorporated in Darcy's law. The dataset for the extrapolation was based on Table 3. Using the flow characteristics measured from the experiments the gas permeability is calculated for higher temperatures. The need for such an estimation comes from the fact that the actual gases evolving during the casting process are higher than room temperature. The dynamic viscosity of a fluid affects the way it flows through the pores and the pressure difference it creates when it flows from one end to the other. Hence during the gas evolution process, when the high temperature volatile compounds try to escape the mould/core, the effect of dynamic viscosity must be taken into account. Figure 5 shows the effect of air temperature on the gas permeability which is calculated from the increasing dynamic viscosities of air. The measured permeability values (from the first measurement) of both samples A and B were used for the calculation.

From the results it can be seen that high temperature permeability sensitivity is predominant for Sample A, which had a lower room temperature permeability.

The results show how significantly the temperature of the air passing through the sand grains can affect the gas permeability. During the casting process, the temperature of the gaseous volatile substances releasing can be quite high. From the above results, one can notice that the higher the temperature, the higher the gas permeability. Apart from the effect of the dynamic viscosity, the degradation of the core itself due to the decomposition of the binder system could also change the pore structure of the moulding material, both these factors might have a significant effect the overall permeability of the core. However, in-situ experiments where simultaneous measurement of binder system decomposition and changes in pore structure are not available today, however such understandings are needed to evaluate the significance of the phenomena discussed above. The dynamic viscosity of air increases linearly and hence the gas permeability is also seen to have increased linearly.

Table 3
Effect of air temperature on the permeability of samples

Air temperature [°C]	Dynamic viscosity, [kg/ms]	Permeability k [m^2]	
		Sample A	Sample B
20	1.82E-05	5.14E-12	1.62E-12
100	3.24E-05	9.12E-12	2.88E-12
200	4.95E-05	1.39E-11	4.39E-12
300	6.87E-05	1.93E-11	6.10E-12
400	8.95E-05	2.52E-11	7.94E-12
500	1.11E-04	3.12E-11	9.85E-12
600	1.35E-04	3.80E-11	1.20E-11
700	1.59E-04	4.47E-11	1.41E-11
800	1.85E-04	5.21E-11	1.64E-11
900	2.12E-04	5.97E-11	1.88E-11
1000	2.39E-04	6.73E-11	2.12E-11

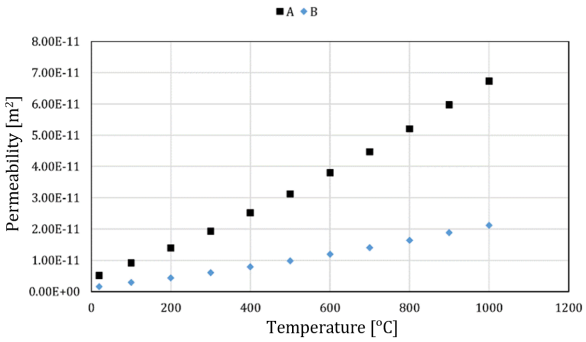

Fig. 5. The effect of air temperature on the gas permeability of the furan sand sample

4.3. MIP results

The results presented below are from the average of two samples from A (A1 and A2) and three samples from B (B1, B2 and B3). The sample A3 is not included in the results because of an unexpected error during the mercury intrusion process. The differential intrusion pore volume plotted against the mean pore diameter (with a logarithmic scale for the mean pore diameter) is shown in Figure 6.

From Figure 6a, it can be seen that both the samples show a bimodal pore size distribution. Both have pores in the size range of 300–0.01 μm. However, Sample B had a significantly higher amount of smaller pores. These smaller pores fall under the mesopores category according to IUPAC [18] classification.

a)

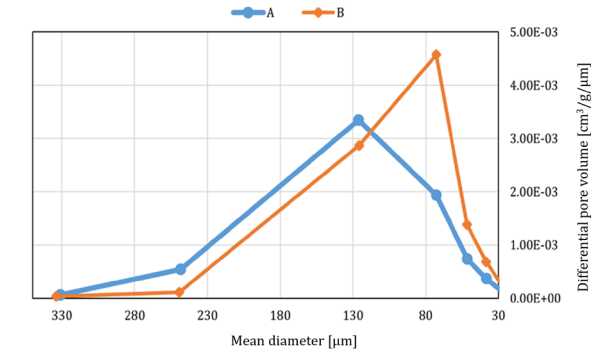

b)

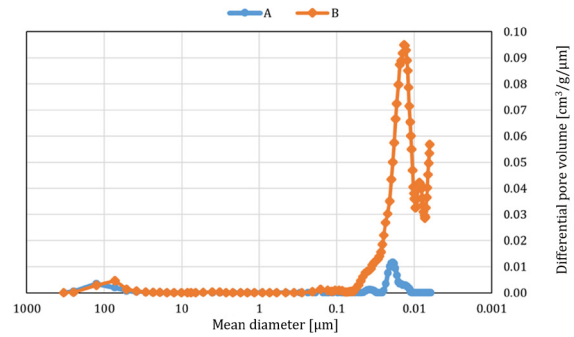

Fig. 6. The differential pore volume curve plotted as a function of the mean pore diameter (a). The first peak of Figure 6a is presented in a linear scale showing the difference in pore (b)

To discuss the pore size distribution more elaborately (Fig. 6b), which had the differential pore volume plotted against the mean pore diameter with a linear axis is presented. The area under the curve represents the pore volume of the sample measured for a particular wide pore radius. Sample B had a lower concentration of larger pores of 230–130 µm. Sample A, on the other hand, had a higher number of larger pores and a lower concentration of smaller pores both in the range of 130–80 µm and 0.1–0.009 µm. The curves showed that, a variation can be observed between sample A and B in terms of the inflection point (which could be considered the critical pore diameter). Sample A had a critical pore diameter of 130 µm, while B had a critical pore diameter of 72 µm. Parameters such critical pore diameter, concentration of the pores and the distribution clearly indicate the difference in pore characteristics and its effect on the permeability of the samples. Sample A which had an overall higher porosity, higher large pore concentration and a higher critical pore diameter exhibited higher permeability. While sample B which had a lower porosity, relatively fewer macropores and a lower critical pore diameter exhibited lesser permeability. It is, however, interesting to see the significantly higher amount of meso-micro pores in Sample B. The effect of these smaller pores on the permeability is also a factor to analyse. Sample B, which had a higher apparent density and greater degree of compaction, exhibits more micropores than Sample A. Cumulative pore volume plots or incremental pore volume plots for the two samples are shown in Figure 7.

It is evident from the cumulative pore volume curve that Sample A had a higher overall porosity and hence higher permeability. Table 4 presents the porosimetry results and the permeability of the specimens. From the results of MIP, it is clear that compaction affects the pore characteristics and the structure of the pores in foundry moulds and cores.

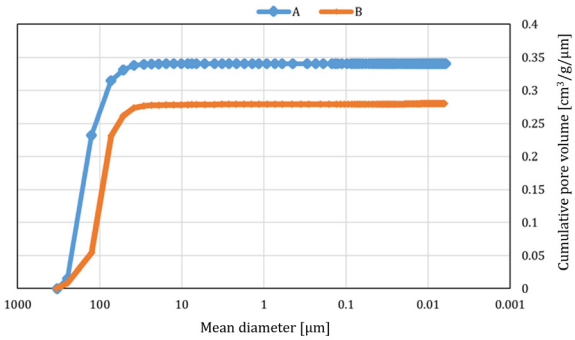

Fig. 7. Cumulative pore volume plots for sample A and B

Table 4
The pore characteristics of the samples measured using mercury intrusion porosimetry

Property	Sample A	Sample B
Apparent density [g/cm³]	1.39	1.51
Pore volume [cm³/g]	0.34	0.27
Median pore diameter [µm]	101	69
Porosity [vol. %]	47.5	43.3
Gas permeability [m²]	$5.26 \cdot 10^{-12}$	$1.43 \cdot 10^{-12}$

5. CONCLUSIONS

The presented work aimed at quantifying gas permeability when the compaction rate varied and samples with varying apparent densities are obtained. The quantification of permeability was done using a custom-made setup that provides results in standard permeability units, square metres [m²]. The results show that the permeability decreased from $5.26 \cdot 10^{-12}$ m² to $1.43 \cdot 10^{-12}$ m² for samples that increased in density from 1.39 g/cm³ to 1.51 g/cm³. The effect of sample density on the permeability was quantified and the reduction in gas permeability was measured in standard units, square metres [m²]. The effect of the temperature of the air on gas permeability was also calculated using the experimental results, with the obtained room temperature gas permeability of one measurement from both Sample A and B. From these results it is clear that gas permeability can significantly increase when air temperature is higher. Hence, when considering the gas permeability values for modelling gas evolution processes in castings, higher gas permeability numbers must be considered so that any underestimation of the amount and rate of gases that the cores could evacuate is avoided.

Results from mercury intrusion porosimetry complimented the results of gas permeability. They showed that the pore characteristics change significantly when the apparent density and compaction is higher for furan no bake sand cores. The number of smaller pores increased significantly with compaction while the critical pore diameter decreased with the increase in apparent density. It not only decreases porosity, but also decreases the average pore size. Porosity affects the permeability at a macro-level, but pore characteristics such as the amount of micro-pores, the diameter of the pores and the interconnectivity of the pores also play an important role in gas permeability. However, it will be interesting to see the effect of increased micro-pores on the gas permeability of foundry samples in the future.

Acknowledgements

The present work is part of the synergy project Lean and sustainable design and production of cast iron components. The work was financed by the Swedish Knowledge Foundation. Cooperating parties in the project are Jönköping University, Scania CV AB, Volvo Group Trucks Technology AB, SKF Mekan AB and SinterCast AB.

REFERENCES

[1] Stoll H. (2009). *Casting design and performance*. Materials Park, OH: ASM International.
[2] Bermudo C., Martín-Béjar S., Trujillo F.J. & Sevilla L. (Eds.). (2019). Use of Additive Manufacturing on Models for Sand Casting Process. *Advances on Mechanics, Design Engineering and Manufacturing II*, 359–369. Doi: https://doi.org/10.1007/978-3-030-12346-8_35.
[3] Campbell J., Svidró J.T. & Svidró J. (2017). Molding and Casting Processes (190–206). In: https://doi.org/10.31399/asm.hb.v01a.a0006297.
[4] Singh R. (2006). *Introduction to basic manufacturing process and workshop technology*. New Delhi: New Age International Pvt Ltd Publishers.
[5] Campbell J. (2003). *Castings*. 2nd Edition. Oxford: Butterworth Heinemann.
[6] Mold & Core Test Handbook. (2001). 3rd Edition. Des Plaines, IL: American Foundry Society.
[7] Ettemeyer F., Lechner P., Hofmann T., Andrä H., Schneider M., Grund D., Volk W. & Günther D. (2020). Digital sand core physics: Predicting physical properties of sand cores by simulations on digital microstructures. *International Journal of Solids and Structures*, 188–189, 155–168.
[8] Pittman E.D. (1992). Relationship of porosity and permeability to various parameters derived from mercury injection-capillary pressure curves for sandstone. *AAPG Bulletin*, 76(2), 191–198. Doi: https://doi.org/10.1306/BDFF87A4-1718-11D7-8645000102C1865D.
[9] Dańko R., Dańko J., Burbelko A. & Skrzyński M. (2014). Core Blowing Process – Assessment of Core Sands Properties and Preliminary Model Testing. *Archives of Foundry Engineering*, 14(1), 25–28.
[10] Dańko R. (2017). Influence of the Matrix Grain Size on the Apparent Density and Bending Strength of Sand Cores. *Archives of Foundry Engineering*, 17(1), 27–30.
[11] Kashif M., Cao Y., Yuan G., Asif M., Javed K., Mendez J.N., Khan D. & Miruo L. (2019). Pore size distribution, their geometry and connectivity in deeply buried Paleogene Es1 sandstone reservoir, Nanpu Sag, East China. *Petroleum Science*, 16, 981–1000. Doi: https://doi.org/10.1007/s12182-019-00375-3.
[12] Sundaram D., Svidró J.T., Svidró J. & Diószegi A. (2021). On the Relation between the Gas-Permeability and the Pore Characteristics of Furan Sand. *Materials*, 14(14), 3803. Doi: http://dx.doi.org/10.3390/ma14143803.
[13] Sundaram D., Svidró J.T., Diószegi A. & Svidró J. (2021). Measurement of Darcian Permeability of foundry sand mixtures. *International Journal of Cast Metals Research* 34, 97–103. Doi: https://doi.org/10.1080/13640461.2021.1917890.
[14] Winardi L., Littleton H. & Bates C.E. (2005). New Technique for Measuring Permeability of Cores Made from Various Sands, Binders, Additives and Coatings. *AFS Transactions*, 113, 393–406.
[15] Adams T.C. (1925). Testing Molding Sand to Determine Their Permeability. *AFS Transactions*, 32, 114–167.
[16] Sutherland W. (1893). The viscosity of gases and molecular force. *The London, Edinburgh, and Dublin Philosophical Magazine and Journal of Science*, 36(223), 507–531.
[17] Darcy H.P.G. (1856). *Les Fontaines Publiques de la Ville de Dijon*. Paris: Victor Dalmont.
[18] Rouquerol J., Avnir D., Fairbridge C.W., Everett D.H., Haynes J.M., Pernicone N. & Unger K.K. (1994). Recommendations for the characterization of porous solids (Technical Report). *Pure and Applied Chemistry*, 66(8), 1739–1758.

Journal of Casting & Materials Engineering Vol. 6 No. 2 (2022) 39–44
https://doi.org/10.7494/jcme.2022.6.2.39

A Diffusion Model of Binary Systems Controlled by Chemical Potential Gradient

Marek Wróbel, Andriy Burbelko

AGH University of Science and Technology, Faculty of Foundry Engineering, al. A. Mickiewicza 30, 30-059 Krakow
e-mail: marek.wrobel@agh.edu.pl

Received: 31 October 2021/Accepted: 21 March 2022/ Published online: 27 April 2022.
This article is published with open access at AGH University of Science and Technology Press.

Abstract

The paper presents a model of diffusion in a single phase with chemical potential gradient as the driving force of the process. Fick's laws are strictly empirical and the assumption that the concentration gradients are the driving forces of diffusion is far from precise. Instead, the gradient of chemical potential μ_i of component *i* is the real driving force. The matter of governing equations of models that incorporate this approach will be raised and discussed in this article. One of more important features is the ability to acquire results where diffusion against the concentration gradient may occur. The presented model uses the Finite Difference Method (FDM) and employs the CALPHAD method to obtain chemical potentials. The calculations of chemical potential are carried out for instant conditions – temperature and composition – in the entire task domain by Thermo-Calc via a TQ-Interface. Then the heterogeneity of chemical potentials is translated into mass transfer for each individual element. Calculations of two modelling tasks for one-dimension diffusion field were carried out. First: isothermal conditions with linear initial composition distribution and second: constant temperature gradient with uniform chemical composition in the specimen. Results for two binary solid solutions: Fe-C and Fe-Si, in the FCC phase for the given tasks will be presented. Modelling allows us to estimate the time needed to reach a desired state in a particular equilibrium or quasi-equilibrium state. It also shows the path of the composition change during the process. This can be used to determine whether the system at some point is getting close to the formation of another phase due to significant deviation from its initial conditions.

Keywords:

diffusion, modelling, CALPHAD, chemical potential

1. INTRODUCTION

Diffusion is one of the phenomena – alongside electrical conduction with Ohm's law, fluid movement with Poiseuille's law, heat flow with Fourier's law – that follows the general relation of transport that is measured by flux [1, 2]:

$$J_x = -L\frac{\partial A}{\partial x} \tag{1}$$

Although Fick's first law corresponds to Equation (1) it is purely empirical [3, 4] and has limitations in terms of its use. From the fundamental point of view, the assumption that the concentration gradients are the driving forces of diffusion in a multicomponent system is not correct. Instead, the gradient of chemical potential μ_i of component *i* determines the net flow of that element [5]:

$$J_x = -B_i c_i \frac{\partial \mu_i}{\partial x} \tag{2}$$

Because determining chemical potential was perhaps not the most convenient way of dealing with the diffusion problem, it was better to express flux entirely in terms of concentration. Since $\mu_i = -\mu_i^0 + RT\ln c_i$, rewriting Equation (2) for uniform temperature gives:

$$J_x = -B_i RT\frac{\partial c_i}{\partial x} \tag{3}$$

and employing the Nernst–Einstein relation [4]:

$$D_i = B_i RT \tag{4}$$

gives Fick's first law:

$$J_x = -D_i\frac{\partial c_i}{\partial x} \tag{5}$$

Analysing the path of the random walk of the particle allows to calculate mean square displacement and with it,

using the Einstein–Smoluchowski Equation [6] – diffusion coefficient [7]:

$$\left\langle x^2 \right\rangle = 2Dt \tag{6}$$

Fick's first law, however, applies to diffusion events where the rate of transport is steady state; that is the rate of flux is constant [8]. For that reason, the phenomenological relation given by Equation (2) was used in the model.

2. FDM MASS TRANSPORT EQUATIONS

Below is the derivation of general formula for mass transport for three-dimension calculations. Its special case for one-dimension is incorporated into the model presented in this paper.

According to the divergence theorem [9], for any closed space with volume V and external surface S total mass of an element m_i can be calculated by integration over volume of this body:

$$m_i = \iiint_V m_i \, dx \, dy \, dz \tag{7}$$

and the rate of change of that mass by integrating over its surface:

$$\frac{\partial m_i}{\partial \tau} = \iint_S \mathbf{J}_i \cdot d\mathbf{s} \tag{8}$$

where the operator " $\cdot$ " stands for scalar product. Inputting Equation (2) we get:

$$\frac{\partial m_i}{\partial \tau} = -\iint_S B_i c_i \nabla \mu_i \cdot d\mathbf{s} \tag{9}$$

Numerical approximation of Equation (9) can be obtained by replacing differentials with finite differences. In differential calculations, using control volumes method, for finite cuboidal control volume with dimensions Δx, Δy and Δz, this equation converts to (element's index has been dropped):

$$\begin{aligned}
\frac{\Delta m_0}{\Delta \tau} = &-B_{x+}\frac{c_{x+}+c_0}{2}\frac{\mu_{x+}-\mu_0}{\Delta x}\Delta y\Delta z + \\
&-B_{x-}\frac{c_{x-}+c_0}{2}\frac{\mu_{x-}-\mu_0}{\Delta x}\Delta y\Delta z + \\
&-B_{y+}\frac{c_{y+}+c_0}{2}\frac{\mu_{y+}-\mu_0}{\Delta y}\Delta x\Delta z + \\
&-B_{y-}\frac{c_{y-}+c_0}{2}\frac{\mu_{y-}-\mu_0}{\Delta y}\Delta x\Delta z + \\
&-B_{z+}\frac{c_{z+}+c_0}{2}\frac{\mu_{z+}-\mu_0}{\Delta z}\Delta x\Delta y + \\
&-B_{z-}\frac{c_{z-}+c_0}{2}\frac{\mu_{z-}-\mu_0}{\Delta z}\Delta x\Delta y
\end{aligned} \tag{10}$$

where index 0 refers to values of concentration, chemical potential or mobility for the considered cell whereas indexes x, y, z along with signs ± determines values of those quantities for neighbouring cells along given axis and in specified direction. Figure 1 presents the mutual location of the origin cell and its neighbours.

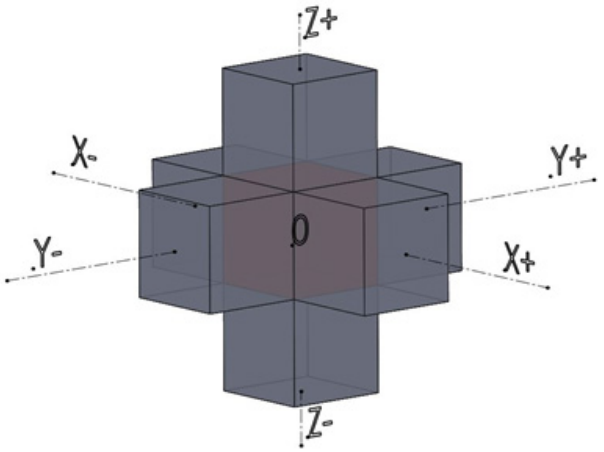

Fig. 1. Mutual location of origin cell 0 and its neighbouring cells $x\pm$, $y\pm$, $z\pm$

For cubic grid with edge Δx Equation (10) can be simplified as:

$$\begin{aligned}
\frac{\Delta m_0}{\Delta \tau} = &-B_{x+}\frac{c_{x+}+c_0}{2}\left(\mu_{x+}-\mu_0\right)\Delta x + \\
&-B_{x-}\frac{c_{x-}+c_0}{2}\left(\mu_{x-}-\mu_0\right)\Delta x + \\
&-B_{y+}\frac{c_{y+}+c_0}{2}\left(\mu_{y+}-\mu_0\right)\Delta x + \\
&-B_{y-}\frac{c_{y-}+c_0}{2}\left(\mu_{y-}-\mu_0\right)\Delta x + \\
&-B_{z+}\frac{c_{z+}+c_0}{2}\left(\mu_{z+}-\mu_0\right)\Delta x + \\
&-B_{z-}\frac{c_{z-}+c_0}{2}\left(\mu_{z-}-\mu_0\right)\Delta x
\end{aligned} \tag{11}$$

With the assumption that mobility B is constant, after rearranging we get:

$$\begin{aligned}
\Delta m_0 = &\frac{-B\Delta x\Delta \tau}{2}\times \\
&\times[\left(c_{x+}+c_0\right)\left(\mu_{x+}-\mu_0\right)+\left(c_{x-}+c_0\right)\left(\mu_{x-}-\mu_0\right)+ \\
&+\left(c_{y+}+c_0\right)\left(\mu_{y+}-\mu_0\right)+\left(c_{y-}+c_0\right)\left(\mu_{y-}-\mu_0\right)+ \\
&+\left(c_{z+}+c_0\right)\left(\mu_{z+}-\mu_0\right)+\left(c_{z-}+c_0\right)\left(\mu_{z-}-\mu_0\right)]
\end{aligned} \tag{12}$$

By shortening the expression we get the following form of the difference equation for the change of mass of an element in time:

$$\Delta m_0 = \frac{-B\Delta x\Delta \tau}{2}\sum_{dir=1}^{p}\left[\left(c_{dir}+c_0\right)\left(\mu_{dir}-\mu_0\right)\right] \tag{13}$$

In the presented model we track the mass of each element in every cell therefore concentration c is a known value. Mobility B is assumed to be constant for each element. It was calculated using Equation (4) using diffusion coefficients given later. Δx and $\Delta \tau$ are respectively space and time grid steps. The problem of employing Equation (13) rests on the ability to determine the values of chemical potential for each element for the given conditions – composition and temperature.

3. CALPHAD CALCULATIONS

The CALPHAD method, taking its name from CALculations of PHAse Diagrams, gives way to determining the state of a system by the means of calculating it. In other words, it is computational thermodynamics, as in the title of reference [10]. The method allows, among the others, to calculate which phases will be stable and what composition they will have in the equilibrium state, what will be values of thermodynamic quantities for a system or a phase. One of the values that can be calculated in this way is chemical potential, in this case using Thermo-Calc Software – a program basing on CALPHAD method. Detailed information about the topic can be found in [10–13].

Since the presented model needs up-to-date values of μ_i, for every calculation timestep, it is not possible to make one-time calculations using Thermo-Calc and incorporate the result into the model's algorithm. There is a need for the constant exchange of data between routines using Equation (13) in the model and the Thermo-Calc program: new, updated masses of elements in the cell are sent – new values of chemical potentials are being received. Thermo-Calc offers three Software Development Kits that allows such communication, with the TQ-Interface used in the present work. A broad description of acquiring data needed by modelling module can be found in a previous work by the authors [14].

Calculations of the chemical potentials used by the model were made using a Thermo-Calc 2019a with TQInterface and thermodynamic database TCFE7.

4. CALCULATION DESCRIPTION

A simulation of one-dimension diffusion field for two binary systems: Fe-C and Fe-Si, was carried out. For each system, two separate calculation tasks were performed:

1) isothermal conditions with linear composition distribution,
2) constant temperature gradient with uniform chemical composition in the specimen.

Due to the significant difference in the values of mobility of carbon and silicon, the total modelled length of the specimen was chosen individually for each system. In both cases the number of grid cells was equal to 100. Temperature and concentration were chosen to put the system within the range of single (FCC) phase in phase diagrams.

Diffusion coefficients, used to determine values of mobility, were calculated with the use of the Arrhenius Equation:

$$D = D_0 \exp\left(\frac{-Q}{RT}\right) \tag{14}$$

The following values of D_0 and Q were used:

- for D_{Fe}: D_0 = 4.085 cm^2 · s^{-1}, Q = 311.1 kJ · mol^{-1}[15],
- for D_C: D_0 = 0.234 cm^2 · s^{-1}, Q = 147.81 kJ · mol^{-1} [15],
- for D_{Si}: D_0 = 0.07 cm^2 · s^{-1}, Q = 243.0 kJ · mol^{-1} [16].

For each system temperature of task (1) was used in the Equation (14), which is also mean temperature of task (2).

4.1. Fe-C system

Table 1 contains values of the parameters used in the calculations. A total length of 50 mm was modelled.

Table 1
Data used for simulation of Fe-C system

Quantity	Value	Unit
Δx	5E-4	[m]
D_{Fe}	7.04156E-17	[m^2 · s^{-1}]
D_C	2.01838E-11	[m^2 · s^{-1}]
For task (1)		
T	1000	[°C]
$c_{C,\,min}$	0.5	[wt.%]
$c_{C,\,max}$	1.0	[wt.%]
For task (2)		
$T_{min\ (x = 0\ mm)}$	950	[°C]
$T_{max\ (x = 50\ mm)}$	1050	[°C]
c_C	0.75	[wt.%]

Figures 2–4 present the results of the simulation for task (1). The composition curves, for $\tau > 0$, in Figure 2 are not symmetrical with respect to the point in the middle of the plot (25 mm, 0.75 wt.% C). The curves close to $\tau = 0$, e.g. curve **b** do not overlap line **a**. Though small, there is non-zero difference of carbon concentration between **a** and **b** across whole distance.

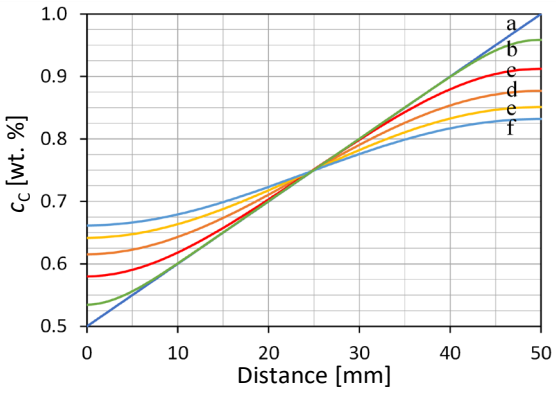

Fig. 2. Initial concentration of carbon (a) and modelled distribution after: b) 5 days; c) 25 days; d) 50 days; e) 75 days; f) 100 days; Fe-C, task (1)

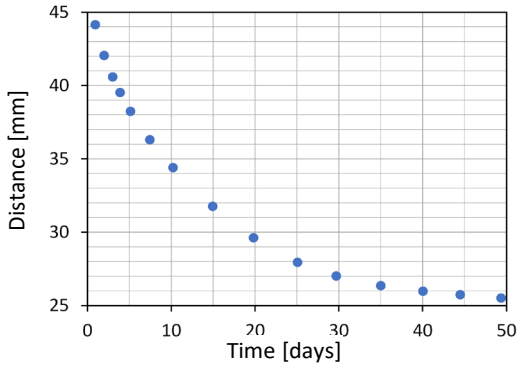

Fig. 3. Position of point with equal to initial concentration of carbon; Fe-C, task (1)

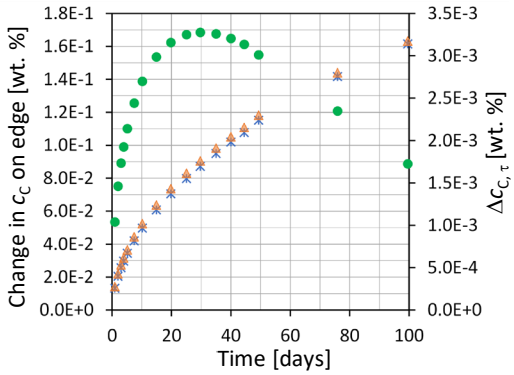

Fig. 4. Change of c_C with respect to initial values for x = 0 (star), x = 50 mm (triangle) and difference of those two (circle); Fe-C, task (1)

Because on one edge c_C with time increases and on the other – decreases the point, where **a** crosses any composition curve for $\tau > 0$, can be distinguished. Figure 3 shows the position of this point of cross where the calculated concentration of carbon is equal to the initial. In early stages it is close to the end with c_C = 1.0 wt.% and in time it asymptotically tends to the middle of the specimen. Figure 4 shows changes in carbon concentration on both edges, at x = 0, x = 50 mm as well as varying difference of those two, defined for element i as:

$$\Delta c_{i,\tau=t_1} = \left|c_{i,\tau=t_0,x=50} - c_{i,\tau=t_1,x=50}\right| + \\ - \left|c_{i,\tau=t_1,x=0} - c_{i,\tau=t_0,x=0}\right| \tag{15}$$

The difference has its maximum at $\tau \approx 30$ days and then slowly decreases as the system tends to equilibrium, where $\Delta c_{C,\tau=\infty} = 0$.

Figures 5–7 present the results for the modelling of task (2). Similarly to task (1), the curves in Figure 5 for $\tau > 0$ are not symmetrical with respect to the point in the middle of the plot (25 mm, 0.75 wt.% C). It is noteworthy that task (2) presents a situation where diffusion occurs with initially zero and shortly even against concentration gradient. A similar uphill diffusion was observed by Darken in [17] for a higher order system. Figure 6 shows the position of a point with equal to initial concentration of carbon. In the early stages it is close to the end with T = 1050°C (x = 50 mm) and in time it asymptotically tends to the point close to the middle of the specimen. In case of task (2) however there is no certainty of final location of that point nor values of $c_{C,x=0}$ and $c_{C,x=50}$ for $\tau = \infty$ as they depend on chosen temperature. Figure 7 confirms that carbon concentrations do not tend to a straight line symmetrical with respect to the middle point as the difference in carbon gain at x = 50 mm and carbon loss at x = 0 cells, within calculated 100 days, constantly increases.

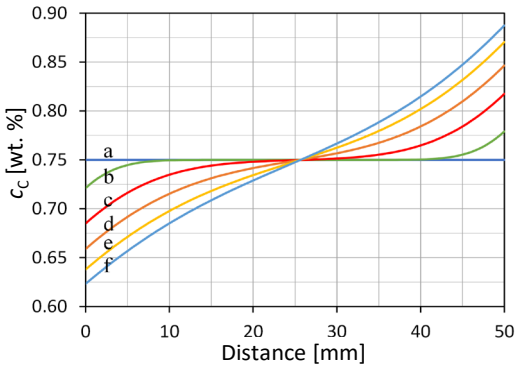

Fig. 5. Initial concentration of carbon (a) and modelled distribution after: b) 5 days; c) 25 days; d) 50 days; e) 75 days; f) 100 days; Fe-C, task (2)

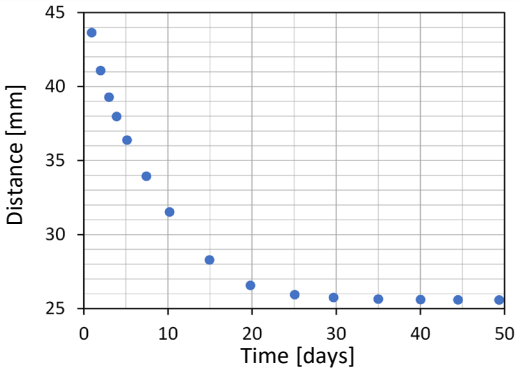

Fig. 6. Position of point with equal to initial concentrations of carbon; Fe-C, task (2)

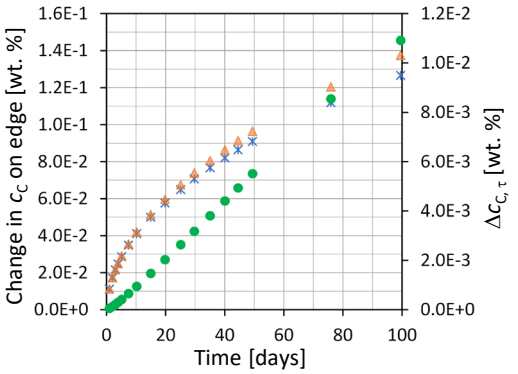

Fig. 7. Change of c_C with respect to initial values for x = 0 (star), x = 50 mm (triangle) and difference of those two (circle); Fe-C, task (2)

4.2. Fe-Si system

Table 2 contains values of parameters used in calculations. A total length of 1 mm was modelled. The results are analogical to the Fe-C system.

Table 2
Data used for simulation of Fe-Si system

Quantity	Value	Unit
Δx	1E-5	[m]
D_{Fe}	3.80618E-15	[m² · s⁻¹]
D_{Si}	1.69443E-14	[m² · s⁻¹]
For task (1)		
T	1200	[°C]
$c_{Si\ min}$	0.05	[wt.%]
$c_{Si,\ max}$	1.55	[wt.%]
For task (2)		
$T_{min\ (x = 0\ mm)}$	1150	[°C]
$T_{max\ (x = 50\ mm)}$	1250	[°C]
c_{Si}	0.80	[wt.%]

Figures 8–10 present results of simulation for task (1). Composition curves, for $\tau > 0$, in Figure 8 are not symmetrical with respect to the point in the middle of the plot (0.5 mm, 0.80 wt.% Si). Figure 9 shows the position of the point with equal to initial concentrations of silicon. In the early stages it is close to the end with c_{Si} = 1.55 wt.% and in time it asymptotically tends to the middle of the specimen. Figure 10 shows varying differences in silicon loss at x = 1.0 mm and silicon gain at x = 0 cells calculated using Equation (15).

It has a maximum at $\tau \approx 15$ days and then slowly decreases as the system tends to equilibrium, where $\Delta c_{Si,\ \tau = \infty} = 0$.

Difference in silicon loss at x = 50 mm and silicon gain at x = 0 cells; Fe-Si, task (1).

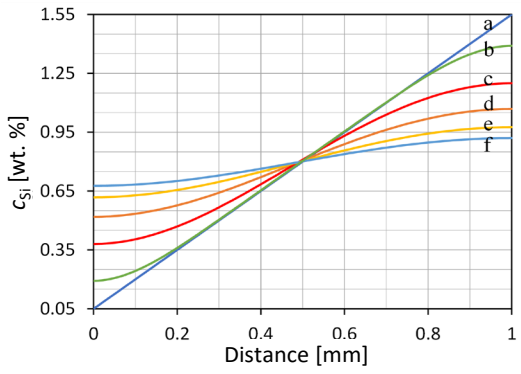

Fig. 8. Initial concentration of silicon (a) and modelled distribution after: b) 5 days; c) 25 days; d) 50 days; e) 75 days; f) 100 days; Fe-Si, task (1)

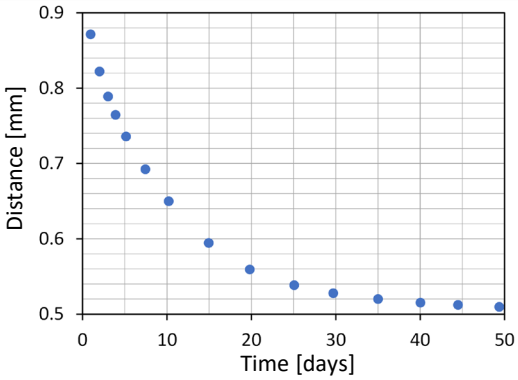

Fig. 9. Position of point with equal to initial concentrations of silicon; Fe-Si, task (1)

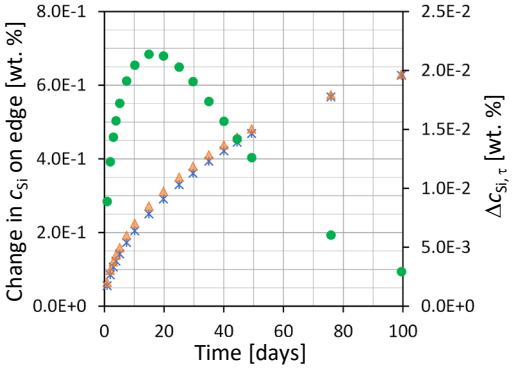

Fig. 10. Change of c_{Si} with respect to initial values for x = 0 (star), x = 1 mm (triangle) and difference of those two (circle); Fe-Si, task (1)

Figures 11–13 present results for modelling of task (2). Similarly to task (1), the curves in Figure 11 for $\tau > 0$ are not symmetrical with respect to the point in the middle of the plot (0.5 mm, 0.80 wt.% Si). Again, it is situation where uphill diffusion occurs. Figure 12 shows position of point with equal to initial concentrations of silicon. In the early stages it is close to the end with T = 1250°C (x = 1.0 mm) and in time it asymptotically tends to the point close to the middle of the specimen. Figure 13 confirms that silicon concentration do not tend to a straight line symmetrical with respect to the middle point as the difference in silicon gain at x = 50 mm and carbon loss at x = 0 cells, within calculated 100 days, constantly increases.

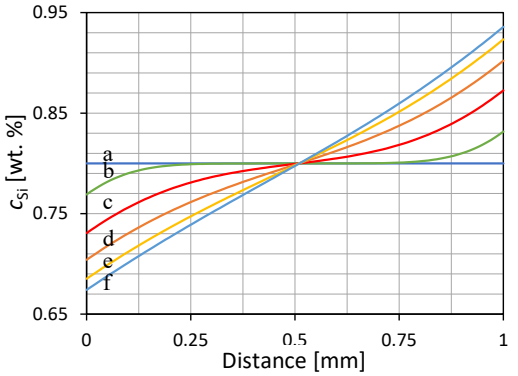

Fig. 11. Initial concentration of silicon (a) and modelled distribution after: b) 5 days; c) 25 days; d) 50 days; e) 75 days; f) 100 days; Fe-Si, task (2)

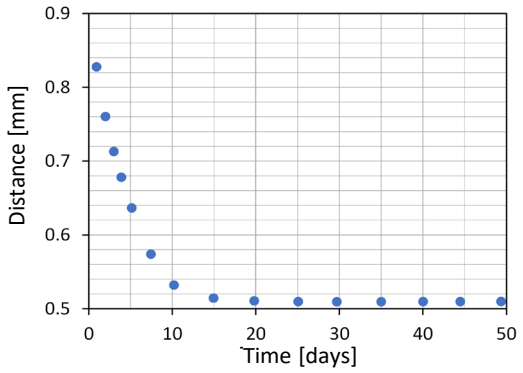

Fig. 12. Position of point with equal to initial concentration of silicon; Fe-Si, task (2)

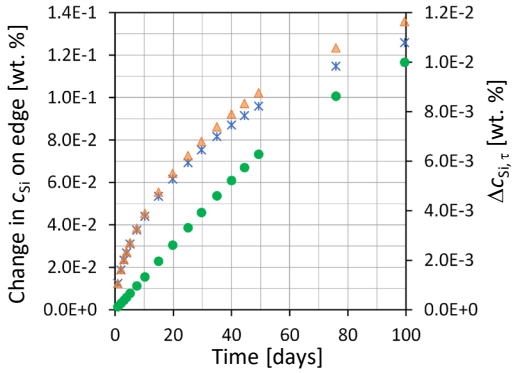

Fig. 13. Change of c_{Si} with respect to initial values for x = 0 (star), x = 1 mm (triangle) and difference of those two (circle); Fe-Si, task (2)

5. CONCLUSIONS

The conditions in which the presented model can be utilised, together with its major features, are summarised below:

- For task (1), the difference in chemical composition in a uniform temperature field leads to the occurrence of chemical potential gradient and non-zero values of fluxes of elements in the system.
- For task (2), the chemical potential gradient is present, despite the initial equality of chemical composition, because of the dependency of chemical potentials on temperature.
- The model uses a single set of equations to determine fluxes for both sources of the difference in chemical potentials.
- For task (2), uphill diffusion (against chemical composition gradient) has been observed, which is not achievable with a model based on Fick's laws.

The model can be used to evaluate the kinetics of changes to a concentration profile for a specimen exposed to non-uniform temperature field which give a view on the time needed to reach a pre-assumed state of interest.

REFERENCES

[1] Bergethon P.R. & Simons E.R. (1990). *Biophysical Chemistry: Molecules to Membranes*. New York: Springer-Verlag.
[2] Shewmon P. (2016). *Diffusion in Solids*. Cham: Springer International Publishers.
[3] Bhadeshia H.K.D.H. (2021). *Course MP6: Kinetics & Microstructure Modelling. University of Cambridge*. Retrieved from: https://www.phase-trans.msm.cam.ac.uk/teaching.html [23.08.2021].
[4] Mehrer H. (2007). *Diffusion in Solids: Fundamentals, Methods, Materials, Diffusion-Controled Processes*. Berlin – Heidelberg: Springer-Verlag.
[5] Porter D.A., Easterling K.E. & Sherif M.Y. (2009). *Phase Transformations in Metals and Alloys.* Boca Raton: CRC Press.
[6] Tilley R.J.D. (2004). *Understanding Solids: The Science of Materials*. Chichester: John Wiley & Sons.
[7] Ernst D. & Kohler J. (2013). Measuring a diffusion coefficient by single-particle tracking: statistical analysis of experimental mean squared displacement curves. *Physical Chemistry Chemical Physics*, 15(3), 845–849. Doi: https://doi.org/10.1039/c2cp43433d.
[8] Bergethon P.R. (2000). *The Physical Basis of Biochemistry*. New York: Springer Science + Business Media.
[9] Spiegel M.R. (1959). *Vector Analysis*. New York: McGraw-Hill.
[10] Lukas H.L., Fries S.G. & Sundman B. (2007). *Computational Thermodynamics*. Cambridge: Cambridge University Press.
[11] Zabdyr L. A. (2005). *Strategia CALPHAD*. Kraków: Instytut Metalurgii i Inżynierii Materiałowej PAN.
[12] Spencer P.J. (2008) A brief history of CALPHAD. *Calphad*, 32(1), 1–8. Doi: https://doi.org/10.1016/j.calphad.2007.10.001.
[13] Wróbel M. & Burbelko A. (2013). Wykorzystanie programów komputerowych do obliczeń termodynamicznych w procesach metalurgicznych: metoda CALPHAD. In: Holtzer M., P*rocesy metalurgiczne i odlewnicze stopów żelaza: podstawy fizykochemiczne.* Warszawa: Wydawnictwo Naukowe PWN, 512–534.
[14] Wróbel M. & Burbelko A. (2014). Retrieval of Thermodynamic Data for Modelling of Solidification Using TQ Interface. *METAL 2014: 23rd International Conference on Metallurgy and Materials,* May 21–23 Brno. (pp. 99-104). Ostrava: Tanger.
[15] Brandes E.A. & Brook G.B. (Eds.) (1998). *Smithells Metals Reference Book*. 7th Edition. Oxford: Elsevier.
[16] Bergner D., Khaddour Y. & Lorx S. (1989). Diffusion of Si in bcc- and fcc-Fe. *Defect and Diffusion Forum*, 66–69, 1407–1412. Doi: https://doi.org/10.4028/www.scientific.net/DDF.66-69.1407.
[17] Darken L.S. (1949). Diffusion of Carbon in Austenite with a Discontinuity in Composition. *Transactions of the AIME*, 180, 430–438.

LIST OF VARIABLES USED IN THE TEXT

$\partial A/\partial x$ – gradient of potential in general flux equation
μ_i – chemical potential of element i
τ – time variable
B_i – mobility of element i
c_i – composition of element i
D_0 – coefficient in Arrhenius Equation
D_i – diffusion coefficient of element i
$_{dir}$ – direction in which neighbouring cell is located: $x\pm$, $y\pm$, $z\pm$
J_x – flux in x direction
L – coefficient in general flux equation
m_i – mass of element i
p – number of directions taking into account in calculations: for model 1D: p = 2, 2D: p = 4, 3D: p = 6
Q – activation energy in Arrhenius Equation
R – gas constant
T – absolute temperature
t – time
x, y, z – space variables

Journal of Casting & Materials Engineering Vol. 6 No. 2 (2022) 45–57
https://doi.org/10.7494/jcme.2022.6.2.45

A Simulation and Experimental Investigation of the Thermal Characteristics of Refractory Bricks Produced Using Fireclay and Agroforestry Wastes

Eugenia Obiageli Obidiegwu*, David Ehigie Esezobor, Henry Ekene Mgbemere, Chiosa Cletus Odili

University of Lagos, Faculty of Engineering, Department of Metallurgical and Materials Engineering, Akoka Lagos, Nigeria
email: eobidiegwu@unilag.edu.ng

Received: 20 October 2021/Accepted: 27 April 2022/Published online: 28 May 2022.
This article is published with open access at AGH University of Science and Technology Journals.

Abstract

Manufacturing and processing industries usually consume large quantities of materials and energy in the course of their operations. The energy supplied for high-temperature processes are used partially for the actual technical process and between 30 to 40% of the energy escapes through the walls of the reactor into the atmosphere, leading to a high degree of thermal inefficiency and fuel consumption. This paper studies the thermal behaviour of insulating refractory bricks produced from a blend of fireclay and agroforestry wastes. The fireclays used were obtained from Ukpor deposit in Anambra State (Latitude 5.95°N, Longitude 6.92°E), Osiele deposit in Abeokuta, Ogun State (Latitude 7.18°N, Longitude 3.45°E) and Kankara Katsina State (Latitude 11.93°N, Longitude 7.41°E), all of which are in Nigeria. Samples were prepared with various weight percentages (60–100 wt.%) clays and (0–40 wt.%) of agroforestry waste, with grain sizes between 212 and 600 μm. Raw materials and the developed refractory bricks were characterised using appropriate standard techniques. The chemical, mineralogical constituents and phases present in the microstructure were examined. Physical and thermo-mechanical properties were investigated. The insulating refractory bricks developed have porosity of 78.83% , cold crushing strength (CCS) 3.144 kN/m^2 and thermal conductivity 0.04–0.046 W/(m·K) that compare favourably with imported bricks 75–85%, 2.756 kN/m^2 and 0.049 W/(m·K) in both physical, mechanical and thermal properties respectively. The reason is that the agroforestry waste used (coconut shell), served to create the pores that improve insulation after burning. Also the ash that remains serves as reinforcement to improve the mechanical properties. The thermal behaviour of the bricks was studied using Finite Element Method and shows a strong correlation with the experimental findings. This indicates that the produced insulating bricks have the thermal properties required for insulation of furnaces.

Keywords:
simulation, insulating bricks, microstructure, thermal characteristics

1. INTRODUCTION

Refractories are materials, which have high temperature and chemical resistance and are used in the insulation of furnaces and kilns against heat loss and chemical damage [1]. Refractory materials retain their shape, strength and chemical identity at high temperature. Refractory bricks play a very important role in the manufacturing industry mainly in the lining of furnaces, kilns, fireboxes and fireplaces. They can be inorganic, non-metallic in nature and depending on how porous they are, can be classified into two categories; dense and porous (insulating) refractories [2]. Insulating refractory bricks also known as porous refractory bricks are usually light in weight, low in thermal conductivity and resistant to high temperature [3].

In developing countries, most refractory bricks are imported and this adversely affects production rate and the cost of the final product. Studies are ongoing on the production of insulating refractory bricks with different combustible materials obtained locally to establish the right proportion to conform to international standards for insulating bricks. An earlier investigation by [4] on the use of coconut shell particulate to enhance the insulating refractory properties of Ukpor, Osiele and Kankara fireclays in Nigeria, showed that clays with 25–30% coconut shell and grain sizes of 212–300 μm fired at 1150–1200°C possessed enhanced physical, mechanical and insulating properties. Also, [5] investigated the effects of coal ash on some of refractory properties of Kankara clay, which has a low refractoriness, thermal resistance and high apparent porosity that are not satisfactory in refractory application. Medium duty fireclay brick capable of possessing good thermal shock resistance was made with the blend at 25 wt.% coal-ash as all the value obtained were within the recommended values for fireclay bricks. In [6], authors evaluated the performance of refractory bricks produced from some local clay deposits in Delta State, Nigeria. After being processed, the clay samples were tested for shrinkage,

bulk density, cold compression strength and thermal shock resistance. The results show that the kaolin deposit at Ogharra was found to be the best material suitable for the lining of the walls of most high thermally operated equipment as its fusion temperature is above the operating temperature of 1200°C. In [2], authors researched on the effects of sintering temperature and agro-wastes on the properties of insulation bricks. In this research, kaolin, ball clay, sawdust and rice husk were used to produce insulation bricks through the solid-state synthesis method. It was found that as the amounts of kaolin used in preparing the samples decreased, the bulk density, modulus of rupture and cold crushing strength (CCS) of the bricks decreased while the water absorption capacity and linear shrinkage increased. The temperature of sintering slightly affected the physical and mechanical properties of the insulation bricks. The samples that were sintered at 1200°C had slightly better properties compared to those sintered at 1100°C.

The need for insulating bricks cannot be over emphasized as several high temperature operations are still ongoing. It has been observed that 30 to 40% of the energy supplied for this operation escapes through the walls into the atmosphere resulting to thermal inefficiency and high fuel consumption [7]. In this research, the thermal characteristics of insulating refractory bricks produced from fireclay and agroforestry waste will be investigated. This is to improve furnace thermal efficiency and thereby reduce high fuel consumption and the cost of production. The aim of this study is to produce refractory bricks with high insulating properties using clays from Nigeria and agroforestry wastes.

2. MATERIALS AND METHODS

2.1. Sample preparation

The materials used for this research are: agroforestry waste (coconut shell) and fireclays collected from Ukpor deposits in Anambra State (Latitude 5.95°N, Longitude 6.92°E), Osiele in Ogun State (Latitude 7.18°N, Longitude 3.45°E) and Kankara Katsina State (Latitude 11.93°N, Longitude 7.41°E), all in Nigeria. The clays used for this study were collected from a depth of 3 meters down the threshold and 6 meters interval using a digger and shovels. The coconut shell (CS), meanwhile, was collected from a coconut chips factory at Ibadan, Nigeria.

The chemical analyses of the as-received materials were conducted using Atomic Absorption Spectrometer (AAS) Perklin Elmer Analyst 200 model at the Chemistry Department, University of Lagos.

The clay and coconut shells were washed, sun dried, crushed with a jaw crusher and ground to finer particles using a ball milling machine at the Federal Institute of Industrial Research, Oshodi (FIIRO). The pulverized materials were sieved using a sieve aperture of 212–500 μm. The sieves were selected after a trial-test. The raw materials were weighed using a METTLER PJ 300 digital weighing machine. Various samples comprising (60–100 wt.%) clays and (0–40 wt.%) of agroforestry waste were produced by mixing clay and agroforestry waste with 40–60 ml of water as shown in Table 1.

Table 1
Mix formulations of the materials (clay and agroforestry waste)

Sample No.	Clays [wt.%]	Agroforestry waste [wt.%]	Clay weight [g]	Agroforestry waste weight [g]
1(Control)	100	0	1000	0
2	95	5	950	50
3	90	10	900	100
4	85	15	850	150
5	80	20	800	200
6	75	25	750	250
7	70	30	700	300
8	65	35	650	350
9	60	40	600	400

The mix formulation was determined through trial-tests. The mould contains a maximum of 1000 g of clay at a time. That was the reason behind using 1000 g for calculating mix formulation.

The compaction was conducted after mixing, in cleaned and oil lubricated moulds of different shapes and sizes (76.2 × 76.2 × 76.2 mm^3, 60 × 60 × 15 mm^3, 50 × 75 mm^2, 95 × 45 × 12 mm^3 and 220 × 110 × 65 mm^3 for CCS, porosity, thermal shock resistance, linear shrinkage tests and for standard bricks respectively).

Various tests were carried on the produced samples.

2.2. Sample characterisation

2.2.1. Physical properties

Bulk density: The bulk density test was carried out by measuring the dry weight of the samples (R) before soaking the samples in hot water for 3 hours and measuring the weight (S) after soaking. The suspended weight in water (W) was taken. Thereafter the value of the bulk density was calculated using Equation (1):

$$\text{Bulk density} = \frac{\rho \times R}{S - W} \tag{1}$$

Apparent porosity: The apparent porosity of the samples were measured according to [8] standard. The value was calculated using Equation (2):

$$\text{Apparent porosity} = \frac{S - R}{S - W} \times 100\% \tag{2}$$

2.2.2. Mechanical property

Cold crushing strength (CCS) is the amount of load that refractory material could withstand after it has been fired to a temperature of 1200°C. This was carried out in accordance with [9] standard, the value was calculated using Equation (3):

$$\text{Cold crushing strength} = \frac{\text{maximum load}}{\text{crossectional area}} \tag{3}$$

2.2.3. Thermal properties

Linear shrinkage: This was carried out in accordance with [10] standard. The value was calculated using Equation (4):

$$\text{Linear shrinkage} = \frac{(l_o - l_i)}{l_o} \times 100\% \tag{4}$$

where:

l_o – original length,
l_i – final length.

Thermal conductivity: The thermal conductivities of the samples were carried out in accordance with [11]. The test samples were measured using a KD2 Pro Thermal Properties Analyser at the Geology Laboratory, University of Ibadan, Nigeria.

Metallographic examination: The micro-structural examination of the samples was carried out using Scanning Electron Microscope (SEM), Zeiss model EVO10, at the Department of Mechanical Engineering Laboratory, the University of Ottawa, Canada.

2.3. Simulation of heat transfer in refractory bricks

The thermal behaviour of the developed brick was conducted using a Finite Element Modelling software (FlexPDE). The rate of heat transfer in the insulating brick was investigated using three bricks with different thermal conductivities.

The mesh grid of the nodes throughout the brick is shown in Figure 1.

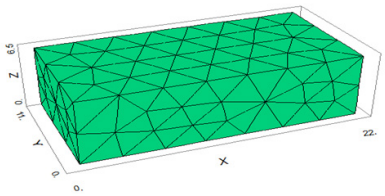

Fig. 1. Mesh grid of 934 nodes through the cross-section of the brick [cm]

The governing equation is given in Equation (5a) and (5b):

$$\frac{\rho C_p}{K_{eff}} \frac{\partial T}{\partial t} = \left[\frac{\partial^2 T}{\partial x^2} + \frac{\partial^2 T}{\partial y^2} + \frac{\partial^2 T}{\partial z^2} \right] \tag{5a}$$

$$K_{eff} = (1 - \varepsilon) K_{solid} + \varepsilon K_{air} \tag{5b}$$

where:

$K_{eff.}$ – effective thermal conductivity,
K_{solid} – thermal conductivity of the solid,
K_{air} – thermal conductivity of the air,
ε – porosity,
C_p – specific heat capacity,
ρ – density of the brick,
T – temperature,
t – time.

The initial conditions inside the furnace were: when $t = 0$, then $T = T_\alpha$, where T_α is the ambient temperature.

Bundary conditions: At the boundary, $t > 0$, $x = 0$, $0 \le y \le B$ and $0 \le z \le H$ the equations explain what happened at each face of the brick during heat transfer; $x = 0$ shows at the beginning of x-axis i.e. in x direction. Also, at the boundary, heat conducted by the brick equals heat loss by convection this is expressed in Equation (6):

$$-K \frac{\partial T}{\partial x} = h_c (T - T_\alpha) \tag{6}$$

Heat conducted by the brick equals heat loss by convection.

At the end of *x*-axis: $t > 0$ (this is at the end of x-axis, when $x = L$), $x = L$, $0 \le y \le B$ and $0 \le z \le H$

where:

L – length of the brick,
B – breadth of the brick,
H – height of the brick,
K – thermal conductivity of the brick,
h_c – convection heat transfer coefficient.

Heat reaching the surface by conduction is equal to heat leaving the surface by convection to the space between two components due to thermal contact resistance this is expressed in the same way as shown in Equation (6).

At the beginning of *y*-axis: $y = 0$, $0 \le x \le L$, $0 \le z \le H$, then heat conducted by the brick equals heat loss by convection as expressed in Equation (7):

$$-K \frac{\partial T}{\partial y} = h'_c (T - T_\alpha) \tag{7}$$

where h' is the face inside the furnace.

At the end of *y*-axis: $t > 0$, $y = B$, $0 \le x \le L$, $0 \le z \le H$, then heat conducted by the brick equals heat loss by convection as expressed in Equation (8):

$$-K \frac{\partial T}{\partial y} = h_c (T - T_\alpha) \tag{8}$$

At the beginning of *z*-axis: $z = 0$, $0 \le x \le L$, $0 \le y \le B$ and the heating element was inserted at this face, then: the quantity of heat from the heating element equals the quantity of heat conducted by the brick as shown in Equation (9):

$$-K \frac{\partial T}{\partial z} = Q'' \tag{9}$$

where Q'' is the quantity of heat from the heating element.

At the end of *z*-axis: $t > 0$, $z = H$, $0 \le x \le L$, $0 \le y \le B$, also the quantity of heat from the heating element equals the quantity of heat conducted by the brick (see Equation (10)).

$$-K \frac{\partial T}{\partial z} = Q'' \tag{10}$$

Table 2
Chemical composition of clay and selected agroforestry waste

Raw materials	Compound [%]									
	Al_2O_3	SiO_2	Fe_2O_3	MgO	CaO	Na_2O	K_2O	TiO_2	H_2O	LOI
Ukpor clay (U)	27.79	53.73	1.24	0.87	0.01	0.56	2.10	0.52	0.003	13.16
Osiele clay (O)	36.23	45.31	0.12	0.52	0.16	0.05	0.04	0.07	0.002	13.06
Kankara clay (K)	25.72	58.84	0.86	0.69	0.24	0.56	1.44	0.34	0.002	7.15
Coconut shell (C)	1.92	2.46	0.24	0.11	0.15	0.20	0.13	0.02	0.001	93.47

3. RESULTS AND DISCUSSION

3.1. Chemical composition

The result of the chemical composition analyses shown in Table 2 indicates that the major constituent of agroforestry waste is organic matter, as captured in the high loss on ignition (LOI) values for the sample. Due to the fact that it is volatile at high temperatures, it is collected as LOI therefore, the agroforestry waste is a carbonaceous material. This can be attributed to the high loss on ignition (LOI) of 93.47% observed in the result. Silica, is also prominent in the waste being the parameter with the highest inorganic content, in the agroforestry waste. It is also the major constituent in the clay which serve as a matrix material. The clay also contains high percentage of alumina, which increases its refractoriness.

3.2. Bulk density

The bulk density values of the samples as a function of the agroforestry waste content are shown in Figure 2. As the amount of waste increased, the density value decreased almost linearly. This property is affected by factors such as nature of the materials blended in the clay sample, particle size, etc. [12]. The nature of materials implies increase in the amount of organic matter present, which leaves air spaces during sintering thereby resulting to decrease in the bulk density values.

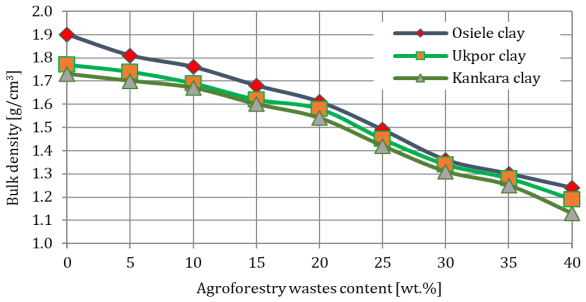

Fig. 2. Variation of bulk density with agroforestry wastes content

3.3. Apparent porosity

The result of apparent porosity is presented in Figure 3. It is observed that as from 25 to 30 wt.% of waste (Fig. 3), there is a sharp increase in porosity followed by a relatively steady portion when compared to the portion below 25 wt.%, this indicates the reasonable amount of agroforestry wastes required. The results obtained show that as the percentage of the waste increases (from 0 to 40 %), the porosity of the samples increases (from 20.07 to 88.09 %, for Osiele clay), (from 31.22 to 89.36 %, for Ukpor clay) and (from 34.10 to 91% for Kankara clay). This can be attributed to the high loss on ignition of the agroforestry wastes, which create void spaces (Tab. 1). This implies that the waste consists of a high amount of combustible material itself, an indication of high porosity. The agroforestry wastes burn off on sintering thereby creating pores, this is in conformity with [12]. The same trend is observed in (Fig. 3). An increase in the grain sizes of the waste, leads to an increase in the porosity of the samples. The values of apparent porosity for the insulating refractory brick samples above 25 wt.% of agroforestry wastes fall within the range of values (75–85%) for insulating bricks according to [8]. This implies that agroforestry waste can be used to improve the insulating properties of clay bricks.

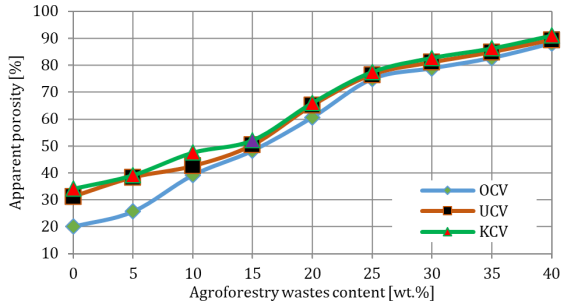

Fig. 3. Variation of apparent porosity of bricks with agroforestry wastes content at 1150°C

Figure 4 shows that thermal conductivity decreases with increase in the weight percentage of the agroforestry wastes. This is attributable to the increase in the formation of pores that hinder heat transfer from one particle to another.

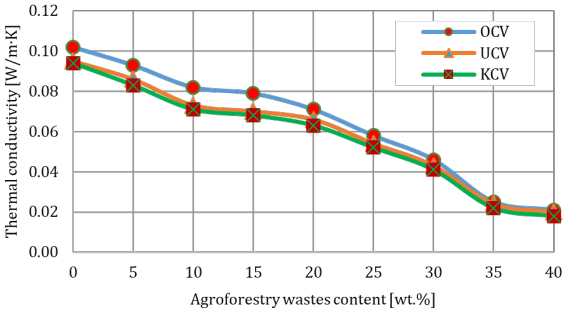

Fig. 4. Variation of thermal conductivity with agroforestry wastes content

Micrographs in Figures 5 and 6 clarify the result by revealing that the pores in the bricks increase with a rise in agroforestry wastes content. When there is an increase in porosity, entrapped air between the particles inhibits the rate of heat transfer leading to a reduction in thermal conductivity [13].

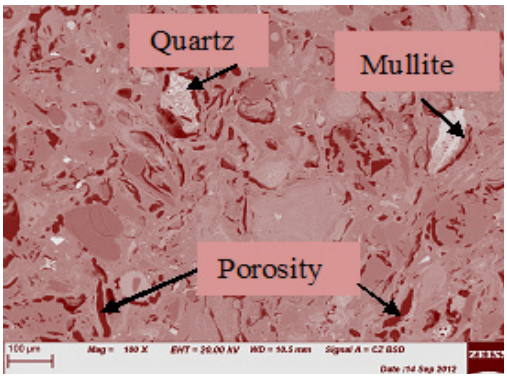

Fig. 5. OT4 (no additive) fired at 1150°C, scale: 100 µm

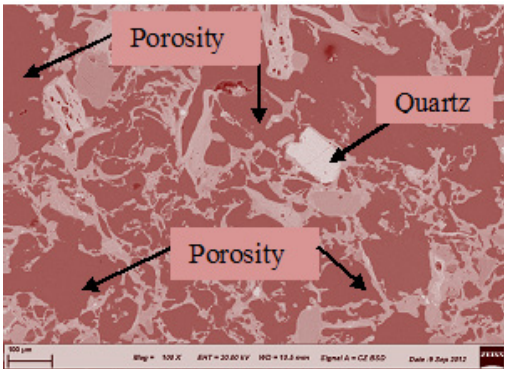

Fig. 6. 1OCXT4 (40% additive) fired at 1150°C, scale: 100 µm

3.4. Cold crushing strength (CCS)

Figure 7 reveals a slight increase in CCS of bricks fired at 950–1000°C due to partial bonding.

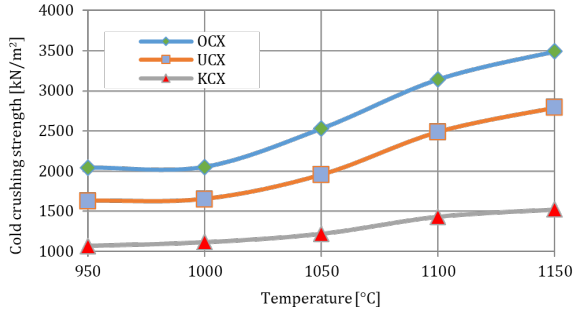

Fig. 7. Variation of CCS with firing temperature of bricks with 30% agrowaste

Between 1000–1100°C, there is a sharp increase in the CCS, which indicates the range of temperature at which considerable bonding occurs between the particles to form a strong coherent body. Meanwhile at a temperature of 1140°C, the increase in CCS tends to be reduced. This is as a result of vitrification that has taken place, during the glassy phase. The degree of variation observed in Figure 7, especially between bricks of Kankara clay and the other clays is as a result of difference in geological history (compositions) of the clays. The CCS of the developed bricks with an admixture of coconut shell and Osiele clay (OCX) as well as Ukpor clay and coconut shell (UCX) are within [9] standards. Bricks produced from Kankara clay, however, have lower strength compared to Osiele and Ukpor clays.

3.5. Simulation of heat transfer in the bricks

Three bricks with thermal conductivities of 0.102 W/(m·K), 0.046 W/(m·K) and 0.049 W/(m·K) and density (ρ) of 2.16, 1.36 and 1.30 g/cm^3 respectively were used. These represent the dense (control) brick without additive (100% clay), the domestically developed porous brick with 30 wt.% of agrowaste and an imported porous brick respectively.

Assumptions made include:

- the thermal properties of the brick are assumed to be constant,
- the brick is to be assumed isotropic,
- the mode of heat transfer in the brick is dominated by heat conduction,
- there is no internal heat generation in the brick.

The heat generated from the heating element installed round the bricks in the furnace are transferred starting from the edges to the core of the bricks as shown in Figure 8.

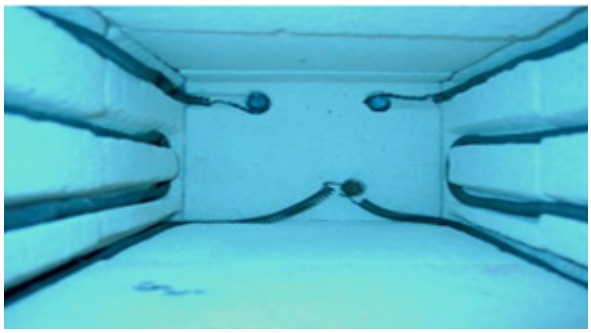

Fig. 8. Installation of heating elements round the bricks

The results of the simulation which revealed the thermal distribution in the bricks at different times are shown in Figures 9–16.

The thermal behaviour of imported porous bricks are similar to that of domestically produced porous bricks containing 30 wt.% of wastes. It takes 9 hours to attain a steady state in the two bricks (Fig. 16a and 16b). But for the domestically produced bricks without any additive (control), it takes only 4 hours (Fig. 14a) to attain a steady state. This confirms that the porous bricks insulate more than the dense bricks due to the large number of pores present in the insulating bricks.

In addition, the longer time to attain a steady state implies low rate of heat transfer, which indicates the high thermal resistance of the porous bricks, thus a reduction in the rate of heat loss through the bricks when installed at the walls of the furnace.

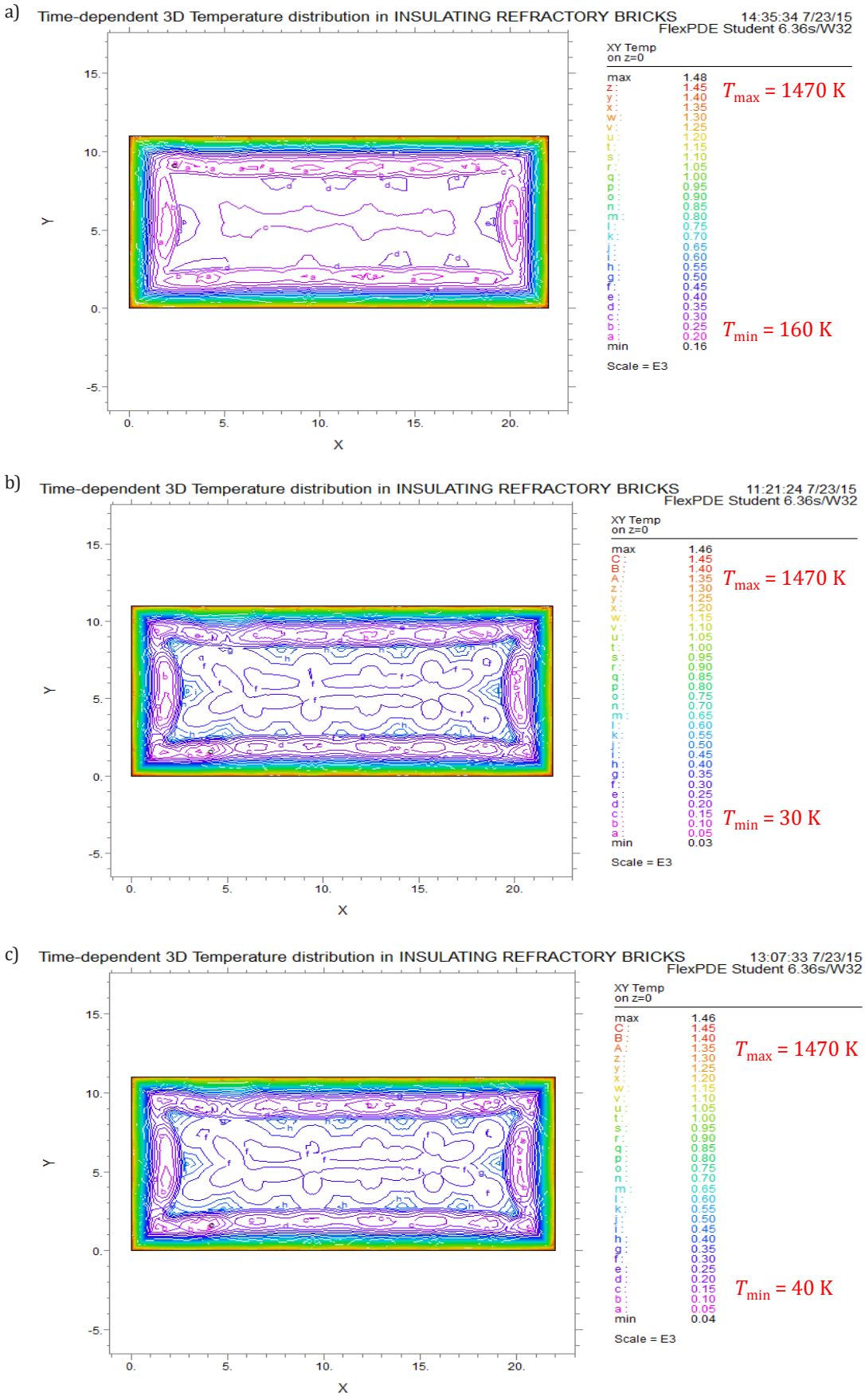

Fig. 9. Graph of heat transfer: a) in brick of 100% clay with K = 0.102 W/(m·K) at 60 s; b) in domestic porous brick with K = 0.046 W/(m·K) at 60 s; c) in imported porous brick with K = 0.049 W/(m·K) at 60 s

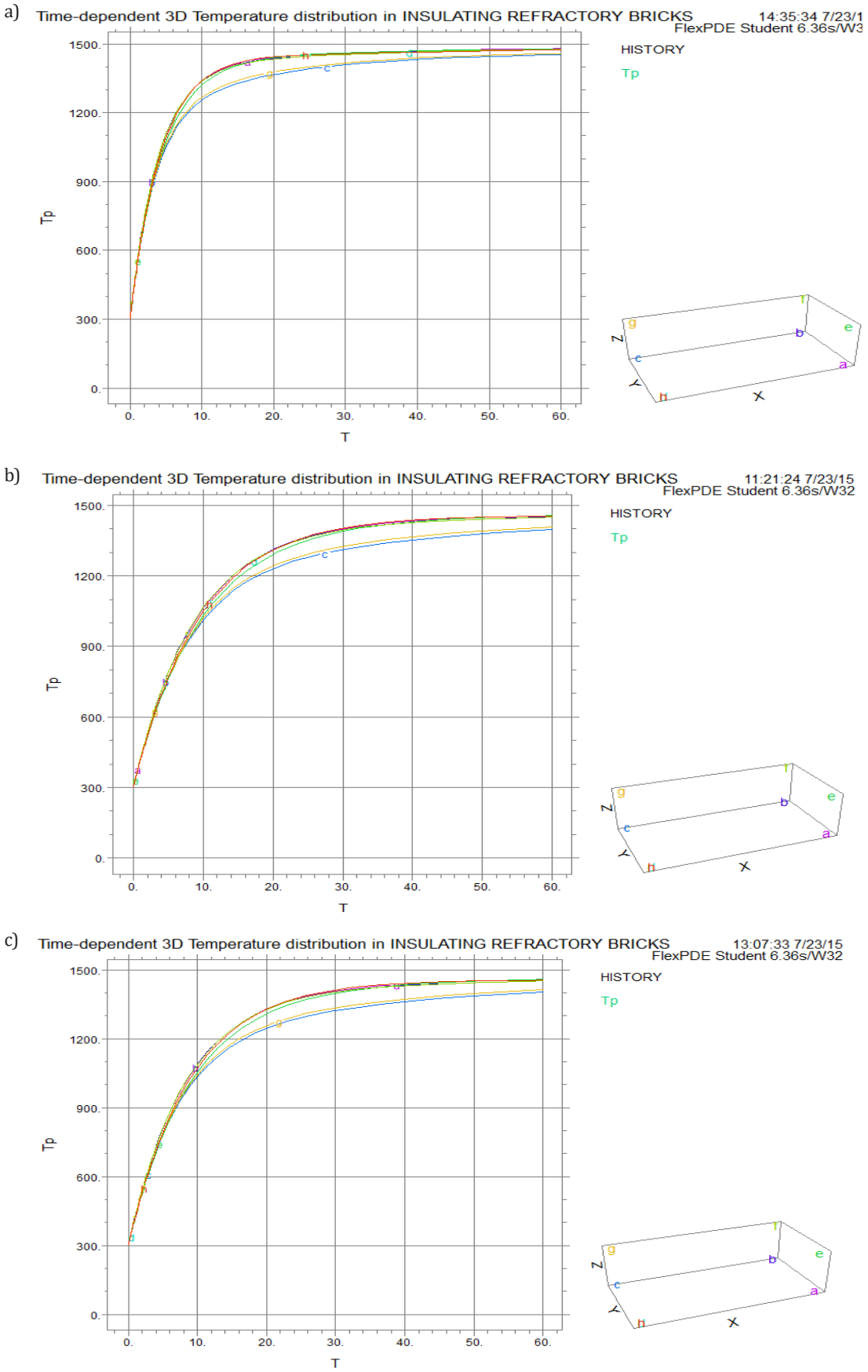

Fig. 10. Graph of heat transfer: a) in domestic dense brick (control) at 60 s; b) in domestic brick with K = 0.046 W/(m·K) at 60 s; c) in imported porous brick at 60 s

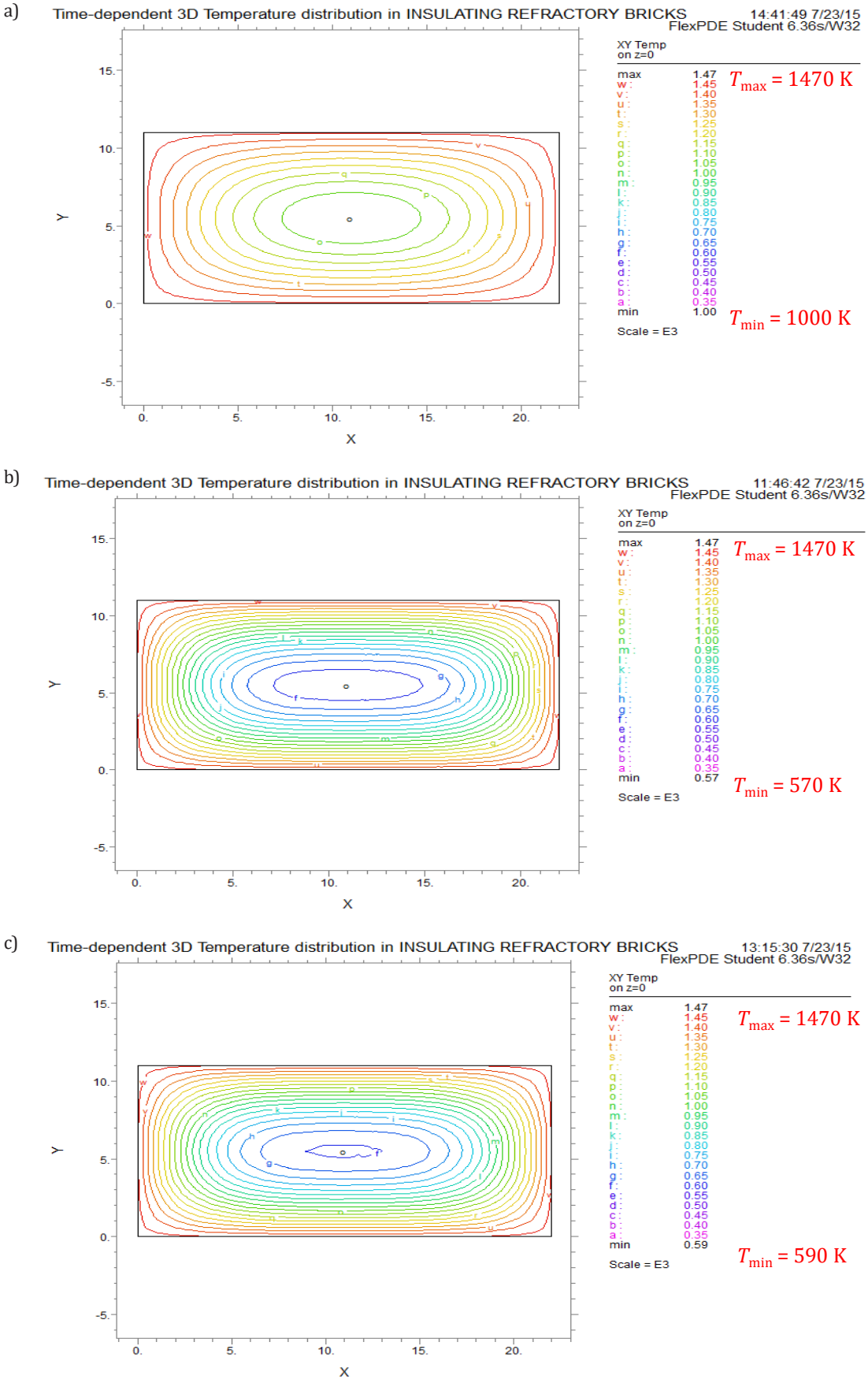

Fig. 11. Graph of heat transfer: a) in domestic dense brick (control) with K = 0.102 W/(m·K) at 1 h; b) in domestic porous brick with K = 0.046 W/(m·K) at 1 h; c) in imported porous brick with K = 0.049 W/(m·K) at 1 h

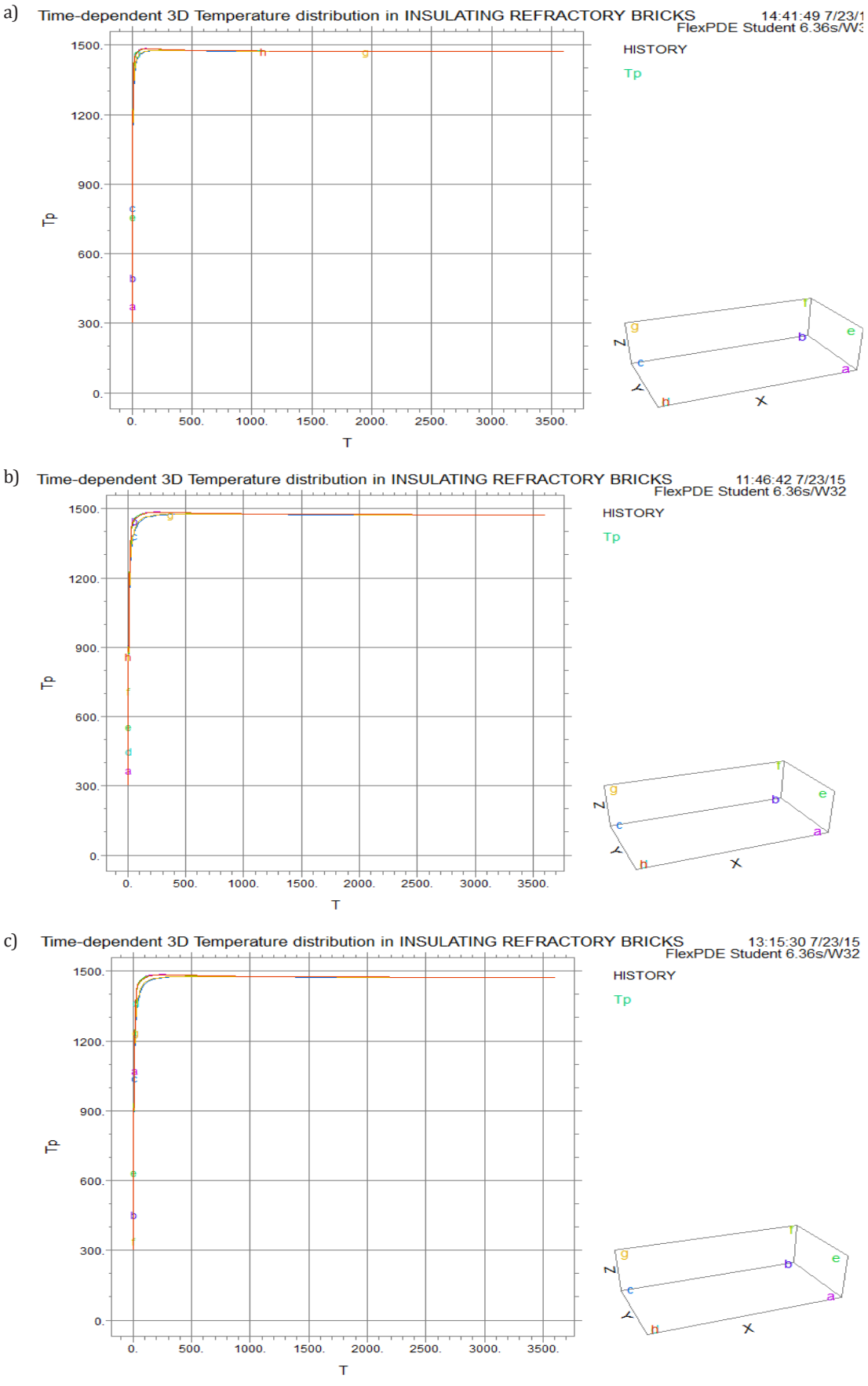

Fig. 12. Graph of heat transfer: a) in domestic dense brick (control) at 1 h; b) in domestic porous brick with K = 0.046 W/(m·K) at 1 h; c) in imported porous brick with K = 0.049 W/(m·K) at 1 h

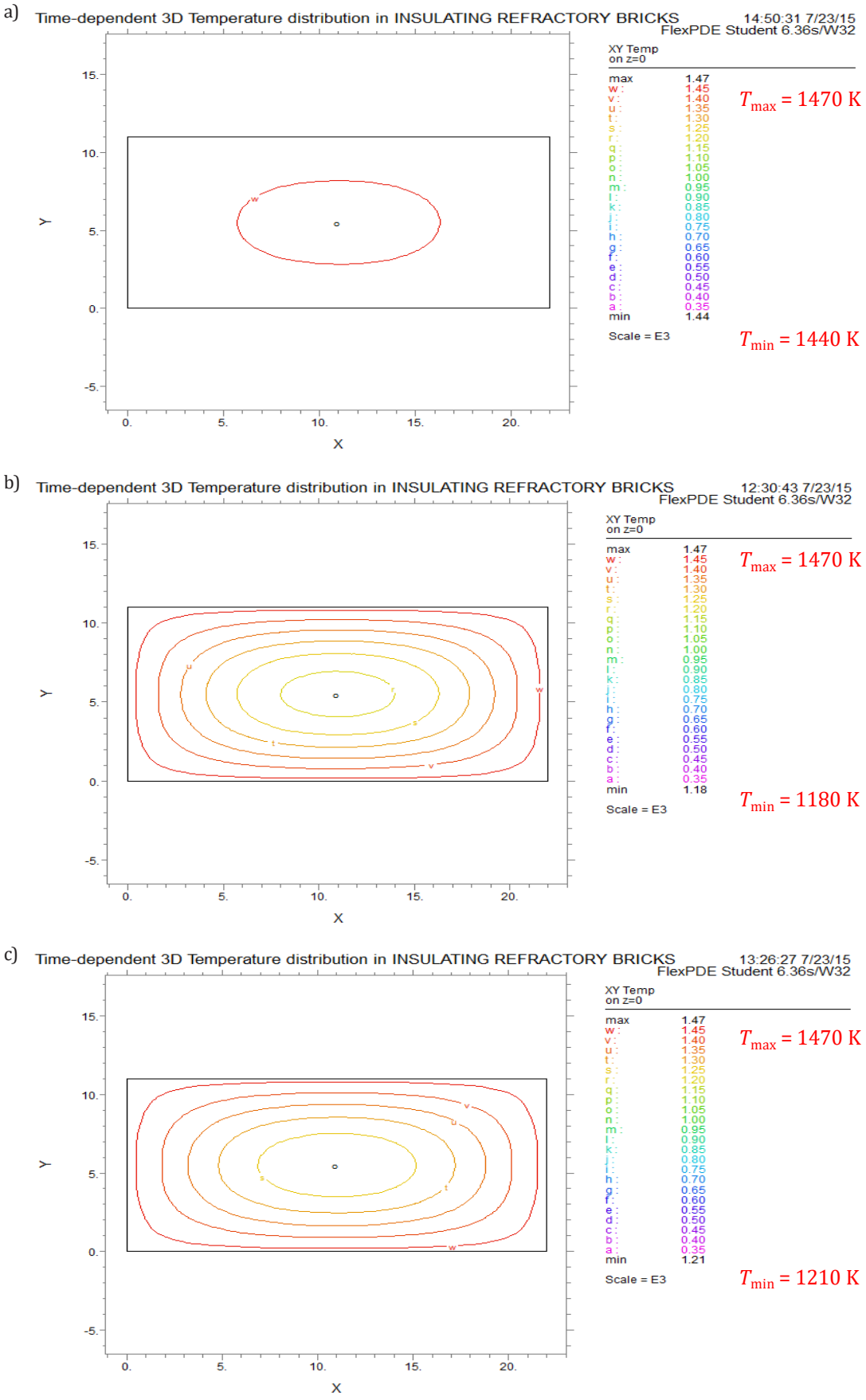

Fig. 13. Heat transfer: a) in domestic dense brick (control) with K = 0.102 W/(m·K) at 3 h; b) in domestic porous brick with K = 0.046 W/(m·K) at 3 h; c) in imported porous brick with K = 0.049 W/(m·K) at 3 h

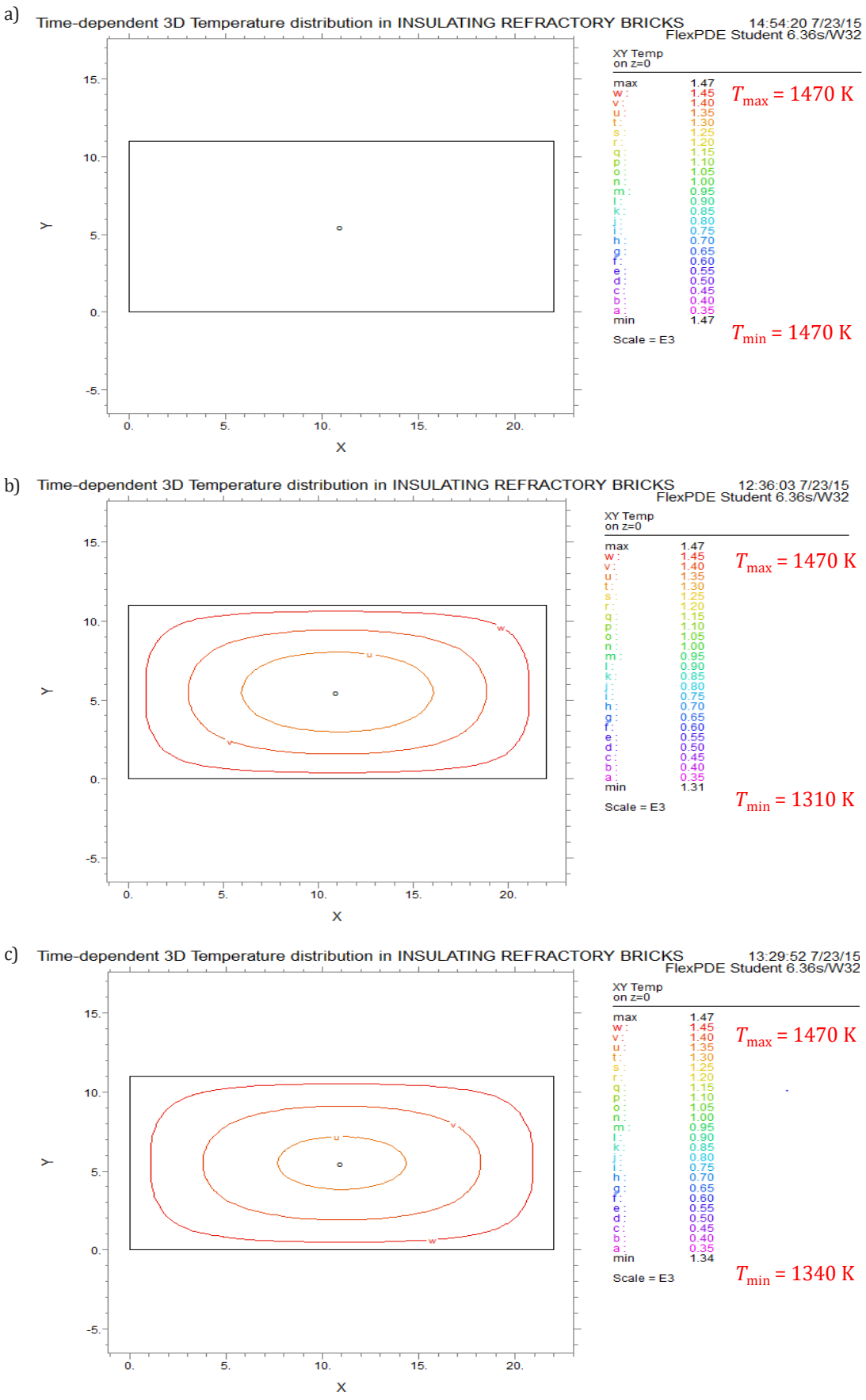

Fig. 14. Heat transfer: a) in dense brick (control) with K = 0.102 W/(m·K) at 4 h; b) in domestic porous brick with K = 0.046 W/(m·K) at 4 h; c) in imported porous brick with K = 0.049 W/(m·K) at 4 h

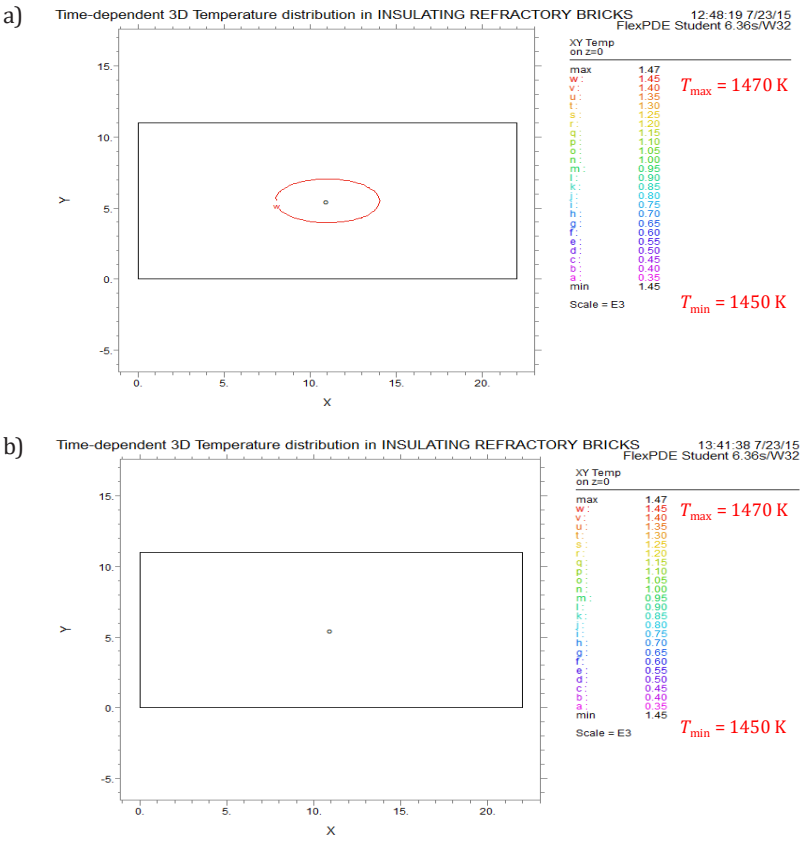

Fig. 15. Heat transfer: a) in domestic porous brick with K = 0.046 W/(m·K) at 7 h; b) in imported porous brick with K = 0.049 W/(m·K) at 7 h

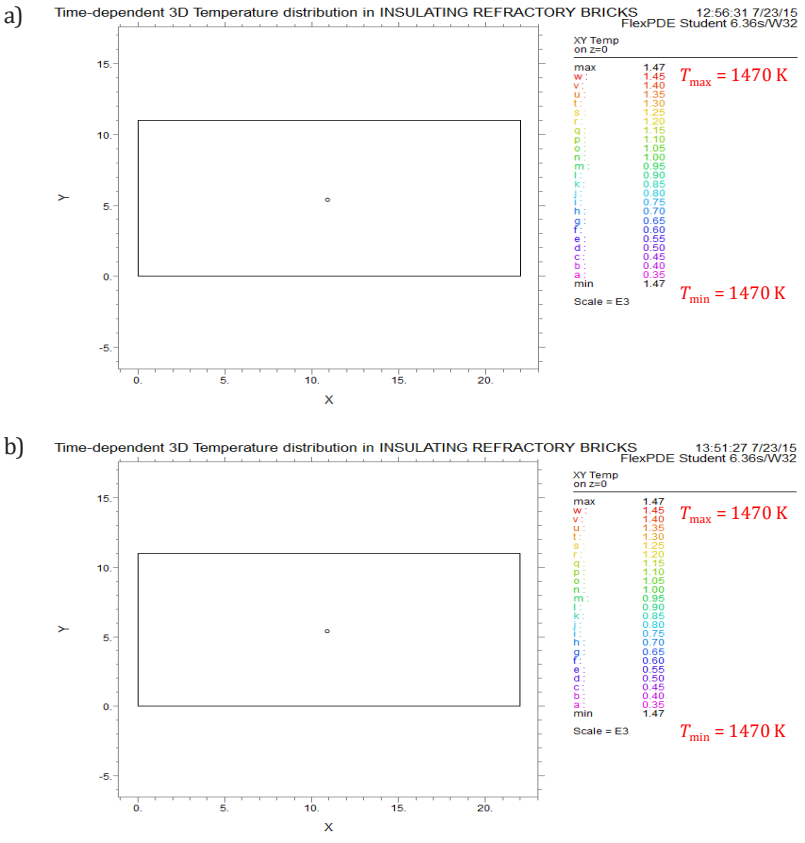

Fig. 16. Heat transfer: a) in domestic porous brick with K = 0.046 W/(m·K) at 9 h; b) in imported porous brick with K = 0.049 W/(m·K) at 9 h

Thus, agroforestry waste can be used to enhance the insulating properties of fireclays.

4. CONCLUSION

This research was carried out to experimentally investigate and simulate the thermal characteristics of refractory bricks produced using Nigerian fireclays and agroforestry wastes. Tests were carried out to study the physical, mechanical and thermal properties, as well as microstructural examinations and simulations.

It can be concluded from the results obtained that, the domestically developed insulating refractory bricks in terms of porosity (78.83%), CCS (3.144 kN/m^2) and thermal conductivity (0.041–0.046 W/(m·K)) compare favourably with imported bricks (75–85%, 2.756 kN/m^2 and 0.049 W/(m·K)) in terms of their physical, mechanical and thermal properties. These values are within the ASTM standard specification of 0.023–0.25 W/(m·K).

In addition, the thermal behaviour of imported porous brick is similar to that of domestically produced porous brick with 30 wt.% of wastes. It takes 9 hours to attain steady state in the two bricks.

Thus, the domestically developed insulating bricks can be used as an alternative to expensive imported bricks in manufacturing and processing industries.

REFERENCES

[1] Odewale I.O., Ameh M.E., Amaakaven V.T.D., Idu F.U., Aluma C.C., Oluwakayode B.J., Abe B. & Ogunkunle D.K. (2020). Effect of Various Combustible Materials on Insulating Properties of Refractory Bricks. *International Journal of Structural Glass and Advanced Materials Research,* 4(1), 168–179. Doi: https://doi.org/10.3844/sgamrsp.2020.168.179.

[2] Mgbemere H.E., Obidiegwu E.O. & Ubong A.U. (2020). The Effects of Sintering Temperature and Agro Wastes on the Properties of Insulation Bricks. *Nigerian Journal of Technological Development*, 17(2), 113–119. Doi: https://doi.org/10.4314/njtd.v17i2.6.

[3] Obidiegwu E.O., Ochulor E.F. & Mgbemere H.E. (2020). Evaluation of the Thermo-Mechanical Properties of Insulating Refractory Bricks Made from Indigenous Clay Mixed with Gmelina Seed Shells Particulates. *ABUAD Journals of Engineering Research and Development*, 3(2), 19–26. Retrieved from: http://ajerd.abuad.edu.ng/wp-content/uploads/2020/12/AJERD0302-03.pdf [accessed: 20.02.2012].

[4] Obidiegwu E.O., Esezobor D.E., Agunsoye J.O. & Lawal G.I. (2015). Enhancement of Insulating Refractory Properties of Selected Nigerian Fire-Clays Using Coconut Shells. *Journal of Minerals and Materials Characterization and Engineering*, 3(6), 458–468. Doi: https://dx.doi.org/10.4236/jmmce.2015.36048.

[5] Hassan S.B. & Aigbodion V.S. (2014). Effect of Coal Ash on Some Refractory Properties of Alumino-Silicate (Kankara) Clay for Furnace Lining. *Egyptian Journal of Basic and Applied Sciences*, 1(2), 107–114. Doi: https://doi.org/10.1016/j.ejbas.2014.04.001.

[6] Osarenmwinda J. & Abel C.P. (2014). Performance Evaluation of Refractory Bricks Produced from Locally Sourced Clay Materials. *Journal of Applied Sciences and Environmental Management*, 18(2), 151–157. Doi: https://doi/org/ 10.4314/jasem.v18i2.1.

[7] Bhatia A. (2011). *Overview of Refractory Materials*, pp. 10–54. Retrieved from: www.phdonline.org [accessed: 20.02.2012].

[8] ASTM C20-00 (2015). Standard Test Methods for Apparent Porosity, Water Absorption, Apparent Specific Gravity and Bulk Density of Burned Refractory Brick and Shaped by Boiling Water. ASTM International, West Conshohocken, PA. Retrieved from: https://webstore.ansi.org/standards/astm/astmc20002015 [accessed: 20.02.2012].

[9] ASTM C133-97 (2015). *American Standard Test Methods for Cold Crushing Strength and Modulus of Rupture of Refractories,* ASTM International, West Conshohocken, PA. Retrieved from: https://www.document-center.com/standards/show/ASTM-C133 [accessed: 20.02.2012].

[10] ASTM C356-17 (2017). Standard Test Method for Linear Shrinkage of Preformed High Temperature Thermal Insulation Subjected to Soaking Heat. ASTM International, West Conshohocken, PA. Retrieved from: https://www.document-center.com/standards/show/ASTM-C356 [accessed: 20.02.2012].

[11] ASTM C182-88 (2013). *American Standard Testing and Materials, test method for thermal conductivity.* ASTM International, West Conshohockon, PA. Doi: https://doi.org/10.1520/C0182.

[12] Ibitoye S. & Alo O. (2014). Adaptation of Odolewu Clay for Use as Refractory Material. *International Journal of Scientific & Engineering Research, 5*(4), 837–843. Retrieved from: https://www.ijser.org/researchpaper/Adaptation-of-Odolewu-Clay-for-Use-as-Refractory-Material.pdf [accessed: 20.02.2012].

[13] Aramide F.O. (2012). Production and Characterisation of Porous Insulating Fired Bricks from Ifon Clay. *Journal of Minerals & Materials Characterization and Engineering*, 11(10), 970–975.